R-Parity Violating Slepton Production and Decay into Two Muons and Jets at $\sqrt{s} = 13$ TeV with CMS

von

Sebastian Wiedenbeck

Bachelorarbeit in Physik

vorgelegt der

Fakultät für Mathematik, Informatik und Naturwissenschaften der RWTH Aachen

im Februar 2016

angefertigt im

III. Physikalisches Institut A

bei

Prof. Dr. Thomas Hebbeker

Eidesstattliche Versicherung

Name, Vorname

Matrikelnummer (freiwillige Angabe)

Ich versichere hiermit an Eides Statt, dass ich die vorliegende Arbeit/Bachelorarbeit/ Masterarbeit* mit dem Titel

selbständig und ohne unzulässige fremde Hilfe erbracht habe. Ich habe keine anderen als die angegebenen Quellen und Hilfsmittel benutzt. Für den Fall, dass die Arbeit zusätzlich auf einem Datenträger eingereicht wird, erkläre ich, dass die schriftliche und die elektronische Form vollständig übereinstimmen. Die Arbeit hat in gleicher oder ähnlicher Form noch keiner Prüfungsbehörde vorgelegen.

Ort, Datum

Unterschrift

*Nichtzutreffendes bitte streichen

Belehrung:

§ 156 StGB: Falsche Versicherung an Eides Statt

Wer vor einer zur Abnahme einer Versicherung an Eides Statt zuständigen Behörde eine solche Versicherung falsch abgibt oder unter Berufung auf eine solche Versicherung falsch aussagt, wird mit Freiheitsstrafe bis zu drei Jahren oder mit Geldstrafe bestraft.

§ 161 StGB: Fahrlässiger Falscheid; fahrlässige falsche Versicherung an Eides Statt

(1) Wenn eine der in den §§ 154 bis 156 bezeichneten Handlungen aus Fahrlässigkeit begangen worden ist, so tritt Freiheitsstrafe bis zu einem Jahr oder Geldstrafe ein.

(2) Straflosigkeit tritt ein, wenn der Täter die falsche Angabe rechtzeitig berichtigt. Die Vorschriften des § 158 Abs. 2 und 3 gelten entsprechend.

Die vorstehende Belehrung habe ich zur Kenntnis genommen:

Ort, Datum

Unterschrift

Abstract

This thesis presents the analysis of a R-parity violating slepton production and decay into the final state of two muons and at least two jets using data from the CMS experiment taken in 2015 at the center of mass energy $\sqrt{s} = 13\,\text{TeV}$ with an integrated luminosity of $42\,\text{pb}^{-1}$. The data was compared with Monte-Carlo simulated background and signal samples. Different selection criteria are presented and applied to ensure well reconstructed events and to extract the signal from the background distribution. At various stages, good agreement between data and simulation was observed. After applying all selection criteria, no data event was left.
Additionally, first upper limits on the signal cross section have been set and transformed into upper limits on the λ'_{211} coupling. An extrapolation of these upper limits to higher luminosities has been done and was compared to the 8 TeV analysis.

Contents

1 Theoretical Background

1.1 Standard Model

This section is based on D. Griffiths "Introduction to elementary particles"[1].

The Standard Model of Particle Physics (SM) describes all the elementary particles and their interaction that are known of today. It contains two types of particles, fermions, particles with an half integer spin, and bosons, particles with an integer spin. They make up matter (fermions) and mediate the interactions (bosons). Fermions are sub-divided into two groups: leptons and quarks. Each lepton can be described by its charge and its generation.

generation	lepton	common symbol	mass (MeV)	electric charge
1	electron	e	0.511	-e
	electron neutrino	ν_e	$< 2 * 10^{-5}$	0
2	muon	μ	106	-e
	muon neutrino	ν_μ	< 0.2	0
3	tau	τ	1777	-e
	tau neutrino	ν_τ	<18	0

Table 1.1: Properties of leptons in different generations [1].

Each lepton has a different mass. As one can see in Table 1.1 for each electrically charged lepton there is a non-charged neutrino. In the SM, neutrinos have no mass, but neutrino oscillation shows that they have indeed masses [2] [3] [4]. The discovery of neutrino oscillations was awarded with a Nobel prize in 2015 [5].
The second group, the quarks, are also divided into three generations (Table 1.2). Like leptons, each quark has a different mass. The electrical charge

	quark	common symbol	mass (MeV)	electric charge
1st generation	up	u	2	$\frac{2}{3}e$
	down	d	5	$-\frac{1}{3}e$
2nd generation	strange	s	100	$\frac{2}{3}e$
	charm	c	1200	$-\frac{1}{3}e$
3rd generation	top	t	174000	$\frac{2}{3}e$
	bottom	b	4200	$-\frac{1}{3}e$

Table 1.2: Properties of quarks in different generations [1].

differs between two thirds and negative one third of the elemental charge e.

There are four known fundamental interactions in nature, see Table 1.3.

Interaction	Strength	Theory	Mediator
Strong	10	Chromodynamics	Gluon g
Electromagnetic	10^{-2}	Electrodynamics	Photon γ
Weak	10^{-13}	Flavourdynamics	W and Z
Gravitational	10^{-42}	Geometrodynamics	(Graviton)

Table 1.3: Known fundamental interactions in nature [1].

Only the first three interactions are part of the Standard Model and are described using quantum field theories where particles are treated as excited states of physical fields. The construction of a satisfying quantum theory of gravitation is one of the greatest problems of modern physics.

The electromagnetic interaction is described by quantum electrodynamics (QED) which was the first to be developed. In QED, the mediator of the interaction is the photon which is massless and has no self coupling. Therefore the range of the electromagnetic force is infinite.

The next interaction is called strong interaction. It describes the force between quarks using color as a charge which is the reason the theory is called quantum chromodynamics (QCD). The mediator of QCD is the massless gluon. There are three kinds of color in QCD: red, green and blue (each color has an anti-color). The color of a quark can change but because the color is conserved a gluon has to carry away the difference. The gluon itself carries a color charge which results in a coupling to other gluons and explains the short range of this interaction (about 10^{-15} m) even with a massless mediator. Overall, there are 8 different types of gluons($|r\bar{g}\rangle$,$|r\bar{b}\rangle$,$|g\bar{r}\rangle$,$|g\bar{b}\rangle$,$|b\bar{r}\rangle$,$|b\bar{g}\rangle$,$\frac{1}{\sqrt{2}}(|r\bar{r}\rangle - |g\bar{g}\rangle$,$\frac{1}{\sqrt{6}}(|r\bar{r}\rangle + |g\bar{g}\rangle - 2\,|b\bar{b}\rangle)$ in QCD. In nature, only colorless particles have been observed. This means that quarks only appear in colorless packages like two quarks with one quark carrying the anti-color of the other quark (mesons) and three quarks carrying all three different colors or anti-colors (baryon). In July 2015, a paper about the possible discovery of a pentaquark state (all three colors plus one color and its anti-color) was published by LHCb [6]. This leads to the assumption that there is, additional to the mesons and baryons which were already observed, a third state with five quarks (pentaquark).

The last interaction in the SM is called weak interaction. There are two kinds of processes in the weak interaction, the neutral one which is mediated by the non-charged Z^0 boson and the charged one which is mediated by the charged $W^{\pm}$ boson. The range of this interaction is limited to $\mathcal{O}(10^{-18}\,\text{m})$ due to massive mediators.

The electroweak interaction is the unification of the electromagnetic and the weak interaction. In the Standard Model, the electroweak symmetry breaking produces the bosons of the electromagnetic and the weak interaction as mixed

states of the bosons of the electroweak interaction (B, W_1,W_2,W_3).[7]

The last particle in the SM is the Higgs boson. The existence of this particle arises from the introduction of the Higgs mechanism. Without this mechanism there would be no explanation why the W and the Z bosons have mass. The mass of quarks and leptons can be introduced via a new interaction called Yukawa-interaction. With these interactions they couple to the Higgs- field and get a mass. In 2012, the CMS Collaboration and ATLAS published the observation of a new boson with a mass of $m_X = 125$ GeV which seems to have all properties of the Higgs boson [8][9].

Each described particle in the SM has an anti-particle with the same mass and spin but with opposite sign of charge (electric charge, etc.). Therefore, the photon and the Z^0 are their own anti-particle.

1.2 Supersymmetry

Even though the Standard Model describes known particles very well, there are phenomenons in physics that it cannot explain. For example, as mentioned in the previous section, the Standard Model provides no description of gravitational effects. Additionally, observations of the rotation curves of galaxies provide evidence for a new type of matter called "dark matter" which can not be explained within the Standard Model as well[10]. Because of these and other discrepancies between observations and the Standard Model one needs to develop new theories. One promising theory is called supersymmetry (SUSY). Most of this section is based on a pedagogical introduction to supersymmetry [11].

1.2.1 Fundamentals

In Supersymmetry, a new transformation is introduced, which transforms a bosonic particle into a fermionic particle and vice versa. In the Minimal Supersymmetric Standard Model (MSSM) each Standard Model particle has exactly one so called supersymmetric partner or superpartner. The fermionic superpartner of gauge bosons are called gauginos and the partner of fermions are called squarks and sleptons which is short for scalar quarks and scalar leptons. To describe SUSY in QFT, particles are grouped up into so called supermultiplets which are the collection of the associated superpartners. To indicate a supersymmetric particle a tilde above the particle symbol is used (i.e. $\tilde{\mu}$, $\tilde{e}$,...). Table 1.4 shows a collection of the supermultiplets in the MSSM.

In supersymmetry, there are more higgs particle then in the Standard Model. Using the effects of electroweak symmetry breaking, the mixing of the higgsinos and electroweak gauginos is possible. The mixed states from the combination of the neutral higgsinos ($\tilde{H}_u^0$,$\tilde{H}_d^0$) and gauginos ($\tilde{W}^0$,$\tilde{B}^0$) are called neutralinos ($\tilde{\chi}_1^0$,$\tilde{\chi}_2^0$,$\tilde{\chi}_3^0$,$\tilde{\chi}_4^0$) and those from the charged higgsinos ($\tilde{H}_u^+$,$\tilde{H}_d^-$) and

Names		spin 0	spin 1/2
squarks, quarks (x3 families)	Q	$(\tilde{u}_L\ \tilde{d}_L)$	$(u_L\ d_L)$
	$\overline{u}$	$\tilde{u}_R$	u_R
	$\overline{d}$	$\tilde{d}_R$	d_R
sleptons, leptons (x3 families)	L	$(\tilde{\nu}\ \tilde{e_L})$	$(\nu\ e_L)$
	$\overline{e}$	$\tilde{e}_R$	e_R
Higgs, higgsinos	H_u	$(H_u^+\ H_u^0)$	$(\tilde{H}_u^+\ \tilde{H}_u^0)$
	H_d	$(H_d^0\ H_d^-)$	$(\tilde{H}_d^0\ \tilde{H}_d^-)$

Table 1.4: Chiral supermultiplets in the Minimal Supersymmetric Standard Model [11].

Names	spin 1/2	spin 1
gluino, gluon	$\tilde{g}$	g
winos, W bosons	$\tilde{W}^{\pm}\ \tilde{W}^0$	$W^{\pm}\ W^0$
bino, B boson	$\tilde{B}^0$	B^0

Table 1.5: Gauge supermultiplets in the Minimal Supersymmetric Standard Model [11].

gauginos ($\tilde{W}^{\pm}$) are called charginos ($\tilde{\chi}_1^{\pm}$, $\tilde{\chi}_2^{\pm}$).
Until now, no SUSY particle has been observed. This leads to the conclusion that their masses must be higher than the mass of their Standard Model partner. Therefore, supersymmetry is a broken symmetry. Thus, the supersymmetric particles not only differ from their standard model partners in spin but also in mass. Supersymmetry contains many different breaking mechanism. One can reduce the number of parameters by considering only a specific amount of them.
Since total baryon and lepton number violating processes like proton decay (Figure 1.1) have not been observed, a new parity can be introduced.

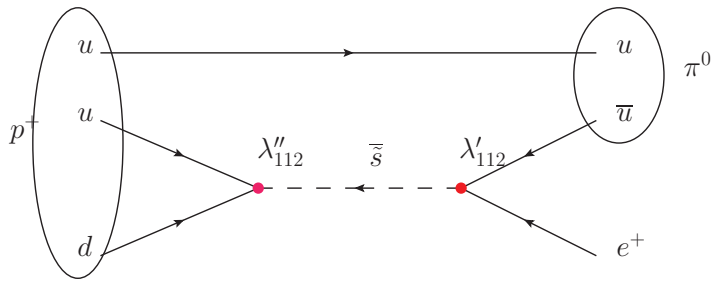

Figure 1.1: Possible proton decay using baryon and lepton number violation. The red points mark the R-parity violating couplings. On the left side, the baryon number is 1 and the lepton number is 0. After the decay, the baryon number is 0 and the lepton number is -1.

A simple conservation of both numbers would not be satisfying because there are electroweak effects which would violate these conservation. The new parity is called R-Parity:

$$P_R = (-1)^{3(B-L)+2s} \tag{1}$$

In Equation 1, s is the spin of the particle, B is the baryon number and L is the lepton number. All Standard Model particles have a R-parity of $P_R = 1$ and all supersymmetric particles have a R-parity of $P_R = -1$. If R-parity is conserved, $P_R = -1$ particles can only be produced in even numbers and the lightest SUSY particle is stable.

The MSSM could also provide a possible grand unified theory (GUT) because of an approximate unification of gauge couplings at a scale of $M_U = \mathcal{O}(10^{16}\ \text{GeV})$ (Figure 1.2).

One can reduce the number of parameters in the MSSM by using only a specific symmetry breaking mechanism. The minimal supergravity (MSUGRA) or Constrained Minimal Supersymmetric Standard Model (CMSSM) reduces the amount of parameters from over 100 to 5 at the GUT scale:

- m_0 : universal scalar particle mass
- $m_{1/2}$: universal fermionic particle mass
- A_0 : trilinear Higgs coupling strength
- $\tan(\beta)$: ratio of the vacuum Higgs expectation value
- $\text{sign}(\mu)$: sign of the bilinear Higgs mixing parameter

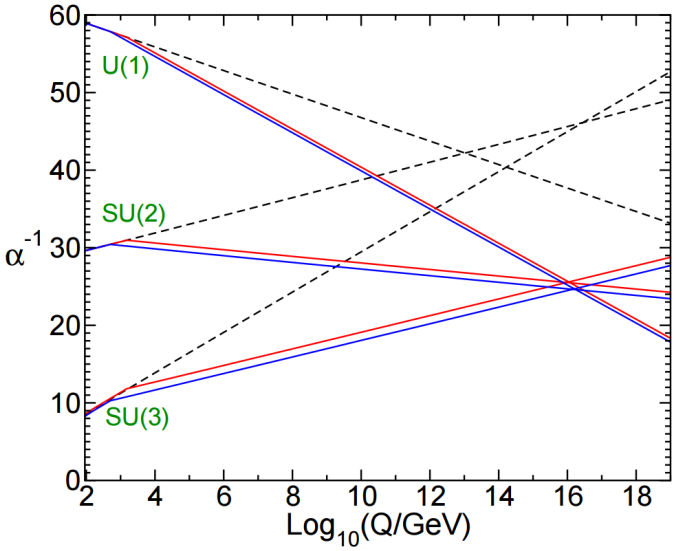

Figure 1.2: Evolution of the inverse gauge couplings α_i. The dashed lines visualizing the Standard Model where the solid lines showing the Minimal Supersymmetric Standard Model.(Taken from [11])

1.2.2 R-Parity Violation

One does not necessarily need R-parity conservation to prevent the proton from decaying. The R-parity violating ($\not{R}_P$) terms in the superpotential are given by [12]:

$$W_{\not{R}_P} = \mu_i H_u L_i + \frac{1}{2}\lambda_{ijk} L_i L_j E_k^c + \lambda'_{ijk} L_i Q_j D_k^c + \frac{1}{2}\lambda''_{ijk} U_i^c D_j^c D_k^c \qquad (2)$$

In Equation 2, H_u is one of the Higgs- superfields, L_i and E_i are the lepton superfields, Q_i, U_i^c and D_i^c are the quark superfields (with the generation index $i = 1,2,3$) and μ_i, λ_{ijk}, λ'_{ijk} and λ''_{ijk} are the couplings of the interactions between the superfields. Combinations of the λ''_{ijk} and the λ'_{ijk} coupling lead to proton decay. To prevent this decay one can introduce a new symmetry called Baryon-triality [13].
Without R-parity conservation the production of single supersymmetric particles from Standard Model particles is possible which leads to new possible production mechanisms and decay chains with final states that can be distinguished well from the Standard Model background.

1.2.3 Resonant Smuon Production

This analysis studies the resonant production of a smuon and muon sneutrino using R-parity violation. Only one coupling of the R-parity violating superpotential is taken into account ($\lambda_{ijk} = \lambda''_{ijk} = 0$, $\lambda'_{ijk} = 0$ for $\{ijk\} \neq \{211\}$). In the simplest graph (see Figure 1.3), a smuon is produced from two quarks then decays into a neutralino $\tilde{\chi}_1^0$ and a muon. The neutralino is not stable and decays into a second muon and an off-shell anti smuon which then decays over the λ'_{211} coupling into two quarks. Other decay chains are possible, for example including a chargino ($\tilde{\chi}_{1,2}^{\pm}$) or heavier neutralinos ($\tilde{\chi}_{2,3,4}^0$). Due to the fact, that neutralinos are majorana particles, probability for two muons with the same charge is about 50 %[14]. The neutralino is considered as the lightest supersymmetric particle (LSP). Also, the resonant production of a sneutrino is possible and can be seen in Figure 1.3.

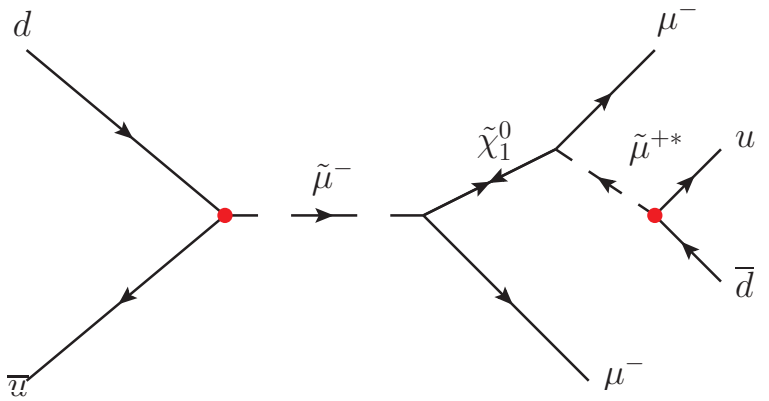

(a) shortest decay chain

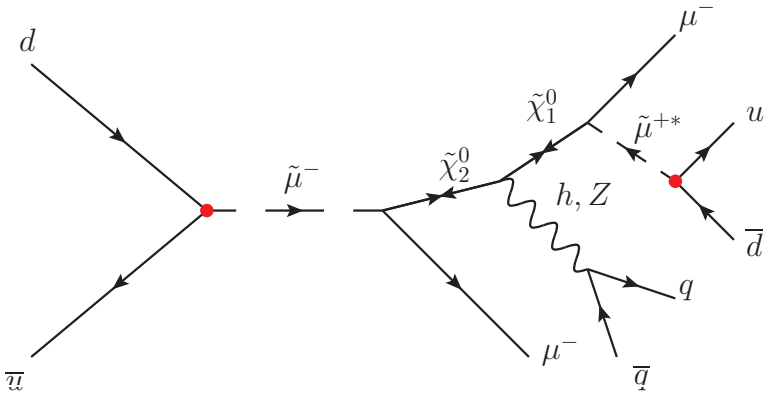

(b) longer decay chain

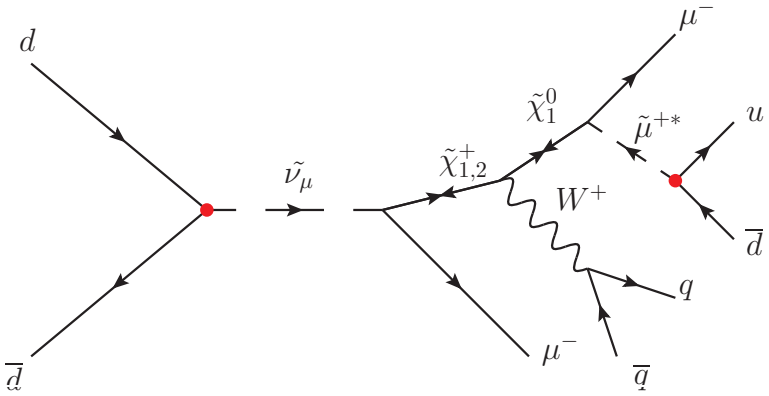

(c) sneutrino decay

Figure 1.3: (a) and (b) show two possible feynman graphs for the resonant smuon production while (c) shows the production of a sneutrino. The R-parity violating vertices are colored in red. At these points, one single supersymmetric particle is produced from two standard model particles or a single supersymmetric particle decays into two standard model particles.

2 Experiment

2.1 The Large Hadron Collider

The Large Hadron Collider (LHC) is the last addition to the accelerator complex of the European Organization for Nuclear Research (CERN) near Geneva and it is designed for a centre-of-mass energy of 14 TeV for colliding protons or 2.8 TeV for Pb ions. It is installed inside a 26.7 km long machine tunnel that was construced for LEP between 1984 and 1989. The tunnel is located up to 170 m below the surface. The particles are accelerated using electric fields and brought to a circular path by superconducting magnets[15].
Several of experiments are installed at the LHC. The four major experiments are A Large Ion Collider Experiment (ALICE), the Large Hadron Collider beauty (LHCb), A Toroidal LHC Apparatus (ATLAS) and the Compact Muon Solenoid (CMS)[16]. Their position at the collider ring can be seen in Figure 2.1. The protons are taken from a bottle with hydrogen atoms. Their

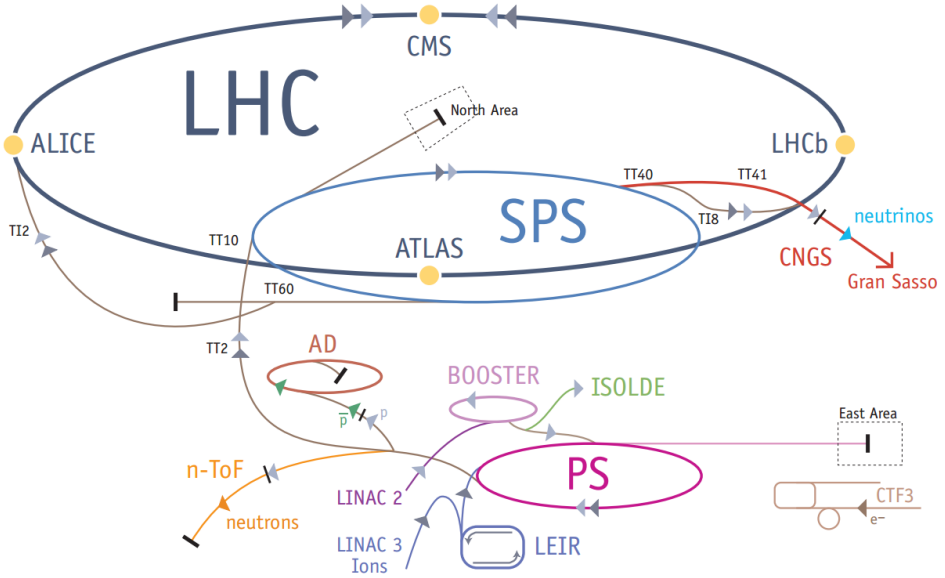

Figure 2.1: Overview of the LHC [17].

electrons have been separated from the nuclei before. This can be done by using a strong electric field which strips the electrons from them. These protons are accelerated to 50 MeV in the LINAC and then are injected into the BOOSTER where they gain an energy of 1.4 GeV. With this amount of energy they reach the Proton Synchrotron (PS), get accelerated to 25 GeV and are sent to the Super Proton Synchrotron (SPS). Finally, the protons arrive at the LHC with an energy of 450 GeV where they reach their maximum energy of 6.5 TeV (2013) [17].

2.2 The CMS Experiment

The Compact Muon Solenoid (CMS) is a detector installed at the LHC. Its purpose is to identify the scatter products from proton-proton, proton-ion and ion-ion collisions. It weighs about 14,000 tons with an overall diameter of 15 m and an overall length of 28.7 m. The magnetic field of the CMS detector has a strength of 3.8 T which is about 100,000 times stronger than the magnetic field of the earth[18].

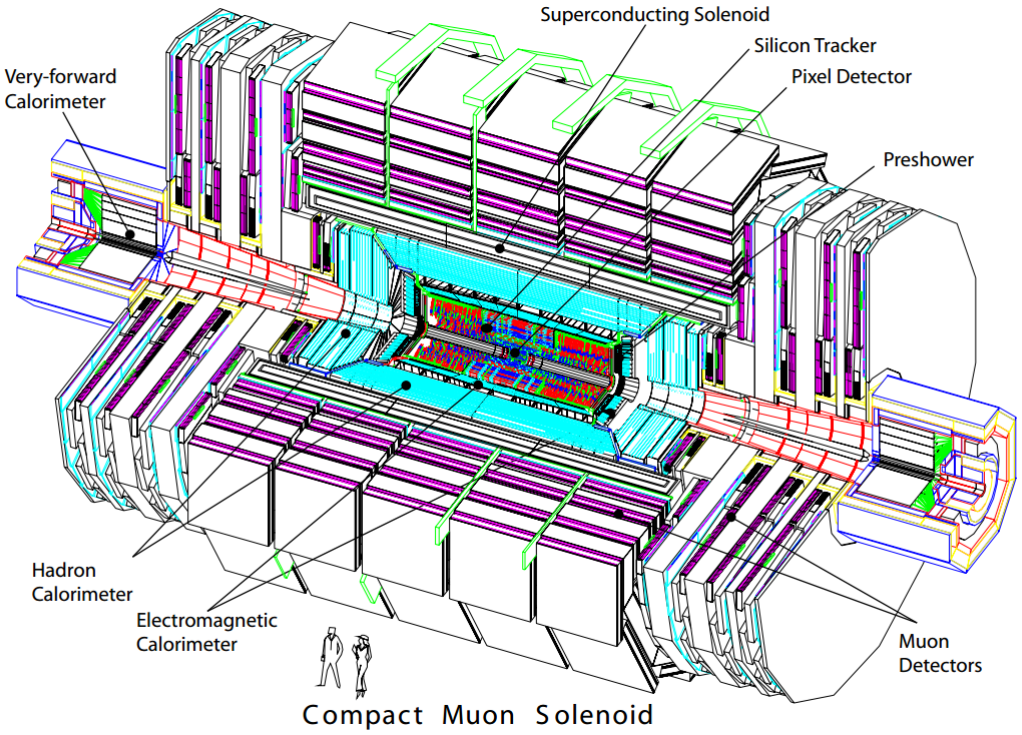

Figure 2.2: Schematic view of the CMS detector design [19].

Figure 2.2 shows the inside of the CMS detector. It is built in layers around the beam pipe. The inner layer contains the inner tracking system which is designed to measure the trajectories of charged particles as well as reconstruct secondary vertices. It is composed of a pixel detector and a silicon strip tracker.
The next layer consists of the electromagnetic calorimeter (ECAL) made of lead tungstate ($PbWO_4$) crystals in the central barrel and the two endcaps and measures the energy of electromagnetic interacting particles.
The next layer is the hadron calorimeter. It is designed for the measurement of hadron jets and other fragments . The hadron calorimeter is extended to the outside of the superconducting solenoid to gain better energy resolution and to identify late starting showers and measure shower energy after the inner hadron calorimeter.
The outer part of the detector contains the muon system. Muons, unlike most

of the other particles, are not stopped by the inner layers and are thus the only particles detected at this region. The multiple layers of the muons system Figure 2.3) are used to reconstruct the path of the muons which gives its momentum. Because of the high strength of the magnetic field of the solenoid even high momenta can be measured[19].
All other particles are measured from their path and their energy.

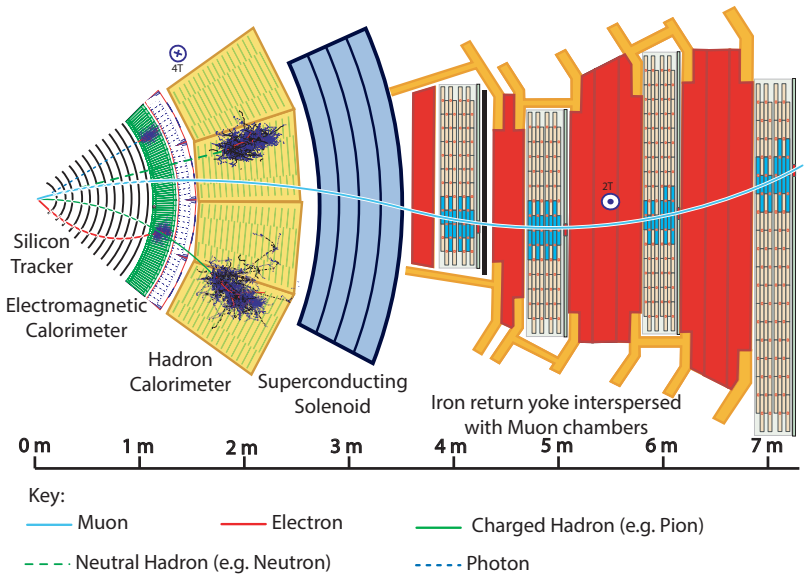

Figure 2.3: Transverse slice through the CMS detector with particle tracks [20].

2.2.1 Event Reconstruction

The detector components provide many information which have to be combined to reconstruct the particles and their properties. For this purpose the particle-flow algorithm [21] is used. It uses all detector parts to identify and reconstruct particles. Then, a collection of these reconstructed particles is used to build jets and calculate the missing transverse energy E_T^{miss}, which contains all particles which are not directly measured with the detector. One can only use the missing transverse energy, because the initial colliding momentum along the z-axis is unknown and therefore the total missing energy can not be reconstructed.
Photons and electrons are reconstructed using the information from the ECAL, where electrons are reconstructed from the electron itself and from photons originating from possible bremsstrahlung and the tracks of the particles.
Muons are reconstructed by combining the tracker and the muon chambers.

Due to the geometry of the CMS detector, a coordinate system has been adopted with its origin at the interaction point. The y-axis is pointing vertically

upward, the x-axis is pointing inward towards the center of the LHC and the z-axis is pointing along the beam direction. Using a spherical coordinate system with the radial coordinate r, the azimuthal angle ϕ,measured from the x-axis, and lying inside the x-y-plane, and the polar angle θ that denotes the angle to the z-axis one can define a so called pseudorapidity η:

$$\eta = -ln(tan(\theta/2)). \tag{3}$$

Differences in η are invariant under longitudinal Lorentz boosts and can be used to describe the distance between two objects:

$$\Delta R = \sqrt{(\Delta\eta)^2 + (\Delta\phi)^2}. \tag{4}$$

The transverse energy $\vec{E_T}$ is defined using θ:

$$\vec{E_T} = \vec{E} \cdot sin(\theta). \tag{5}$$

Also an important quantity is the invariant mass, defined using the absolute value of the four-momentum Equation 6.

$$p \cdot p = \begin{pmatrix} E \\ \vec{p} \end{pmatrix} \cdot \begin{pmatrix} E \\ \vec{p} \end{pmatrix} = E^2 - \vec{p}^2 = m^2. \tag{6}$$

With a number of N particles, the square of the invariant mass of the decaying particle is:

$$M^2 = (\sum_N E)^2 - (\sum_N \vec{p})^2. \tag{7}$$

3 Analysis

3.1 Setup

This analysis is using the TAPAS framework [22]. The main analysis is done with the PxlAnalyser and was computed on a world wide computing grid. For plots, the PlotLib library from TAPAS is used in combination with additional programs using the matplotlib library [23].

3.2 Samples

This section presents the used data samples, background Monte- Carlo simulations (MC) and the signal points.

3.2.1 Data

After a technical stop for upgrading and repairing, the LHC started a new running period in 2015 with a center-of-mass energy of $\sqrt{s}$ = 13 TeV. This analysis uses new data from this run to study sensitivity compared to older 8 TeV analysis. Because this analysis is done during the data taking period one has to find a suitable dataset. At the point in time the single muon dataset from the run B is the most suitable. To calculate the integrated luminosity with brilcalc [24] and to chose properly reconstructed events only, the json file "Cert_246908-251883_13TeV_PromptReco_Collisions15_JSON" is used. This dataset contains all certified events available at that time.

Dataset	Run	$\mathscr{L}_{int}$ $[pb^{-1}]$
/SingleMuon/Run2015B-PromptReco-v1/MINIAOD	251027 - 251883	42.5

Table 3.1: Used Dataset from CMS.

As proton bunches rather than single protons are collided, not only one proton-proton collision happens at each crossing of those bunches (25 ns bunch spacing). This leads to a measurement of more than just one event per crossing. This effect is called Pileup and has to be simulated in the MC. To match the pileup from the data and the MC, a pileup reweighting can be done. In this analysis, no pileup reweighting has been carried out, since the prescription for the reweighting was not yet available at the time of this study.

3.2.2 Reweight

To compare background and signal MC with the data taken in RunB one has to reweight the samples to the correct luminosity. This is done by multiplying the sample cross section σ_{sample} with the integrated luminosity $\mathscr{L}_{int}$ and dividing this product by the absolute event number N_{Events} of the sample:

$$w = \frac{\sigma_{sample} \cdot \mathscr{L}_{int}}{N_{Events}} \tag{8}$$

3.2.3 Monte-Carlo Background Samples

Background Monte- Carlo simulations are produced to differentiate between the measurement of probable new physics and Standard Model processes. For this purpose, official CMS background samples have been used. All MC samples are listed with their cross section and weight in Table 3.2. The weight w is the weight defined in section 3.2.2. The cross sections are taken from [25]. The stars mark their precision where (*) is LO, (**) is NLO, (***) is NNLO and (****) is approx. NNLO.

Table 3.2: Background MC samples with their cross section and weight w.

Group	Background	σ[pb]	weight w
Drell-Yan	$Z/\gamma \to ll$ (10 GeV $< m_{ll} <$ 50 GeV)	18610 (**)	$2.59 \cdot 10^{-2}$
	$Z/\gamma \to ll$ (50 GeV $< m_{ll}$)	6104 (***)	$8.99 \cdot 10^{-3}$
QCD	QCD μ-enr. (15 GeV $< p_T <$ 20 GeV)	1273190000 (*)	68.7
	QCD μ-enr. (20 GeV $< p_T <$ 30 GeV)	558528000 (*)	19.0
	QCD μ-enr. (30 GeV $< p_T <$ 50 GeV)	139803000 (*)	14.2
	QCD μ-enr. (50 GeV $< p_T <$ 80 GeV)	19222500 (*)	3.67
	QCD μ-enr. (80 GeV $< p_T <$ 120 GeV)	2758420 (*)	1.16
	QCD μ-enr. (120 GeV $< p_T <$ 170 GeV)	469797 (*)	$2.66 \cdot 10^{-1}$
	QCD μ-enr. (170 GeV $< p_T <$ 300 GeV)	117989 (*)	$8.57 \cdot 10^{-2}$
	QCD μ-enr. (300 GeV $< p_T <$ 470 GeV)	7820.25 (*)	$8.00 \cdot 10^{-3}$
	QCD μ-enr. (470 GeV $< p_T <$ 600 GeV)	645.528 (*)	$1.74 \cdot 10^{-3}$
	QCD μ-enr. (600 GeV $< p_T <$ 800 GeV)	187.109 (*)	$5.37 \cdot 10^{-4}$
	QCD μ-enr. (800 GeV $< p_T <$ 1000 GeV)	32.3486 (*)	$9.72 \cdot 10^{-5}$
	QCD μ-enr. (1000 GeV $< p_T$)	10.4305 (*)	$3.40 \cdot 10^{-5}$
TTbar	$t\bar{t}$ + jets	670.3 (**)	$3.14 \cdot 10^{-7}$
WJets	W + jets $\to l, \nu$	60290 (***)	$6.86 \cdot 10^{-7}$
DiBoson	WW $\to 2l + 2\nu$	12.178 (***)	$2.68 \cdot 10^{-4}$
	WW $\to 4q$	51.723 (***)	$1.10 \cdot 10^{-3}$
	WW $\to l + \nu + 2q$	49.997 (***)	$1.08 \cdot 10^{-3}$
	WW $\to$ Double Scattering	1.64 (*)	$8.26 \cdot 10^{-5}$
	WZ $\to 3l + \nu$	4.42965 (**)	$9.77 \cdot 10^{-5}$
	WZ $\to l + \nu + 2q$	10.96 (**)	$1.08 \cdot 10^{-6}$
	ZZ $\to 2l + 2q$	3.38 (**)	$1.50 \cdot 10^{-6}$
	ZZ $\to 2q + 2\nu$	4.072 (**)	$7.21 \cdot 10^{-7}$
	ZZ $\to 4l$	1.191 (**)	$2.54 \cdot 10^{-6}$
SingleTop	t (top) (tW-channel)	38.09 (****)	$1.62 \cdot 10^{-3}$
	$\bar{t}$ (antitop) (tW-channel)	38.09 (****)	$1.62 \cdot 10^{-3}$
	t (s-channel)	10.11 (***)	$1.29 \cdot 10^{-4}$
	t (t-channel)	216.99 (***)	$1.14 \cdot 10^{-4}$
Rare Samples	W + W + jj (QCD)	0.01538 (**)	$4.36 \cdot 10^{-6}$
	W + W +jj (EWK)	0.02064(**)	$5.84 \cdot 10^{-6}$

3.2.4 Signal

The signal production was done privately by Philipp Millet with CalcHEP [26] for the core $2 \to 2$ process and Pythia 6 [27] for the decay, showering and hadronization, the mSUGRA model was used with parameters set to: $A_0 = 0$, $\tan(\beta) = 20$ and $\text{sign}(\mu) = 1$. The couplings are set to $\lambda'_{211} = 0.01$, $\lambda'_{ijk} = 0$ for $\{ijk\} \neq \{211\}$, $\lambda_{ijk} = 0$ and $\lambda''_{ijk} = 0$. The lightest supersymmetric particle (LSP) is the lightest neutralino. The signals were produced for 500 GeV $\leqslant m_0 \leqslant$ 2500 GeV and 500 GeV $\leqslant m_{1/2} \leqslant$ 3500 GeV with steps of 500 GeV, rejecting non-physical signal points, e.g. where the neutralino is not the LSP or no electroweak symmetry breaking is happening. This gives a total number of 25 signals. Masses of involved particles rise with with m_0 and $m_{1/2}$, hencing the decreasing cross section. All signal points are visualized in a two dimensional plot and can be found with examples of signal properties in Figure 3.1. Figure (a) shows the cross sections of each produced signal point in the parameter space. (b) gives three examples of the leading muon p_T, (c) for the sub-leading muon p_T and (d) gives the number of muons per event.

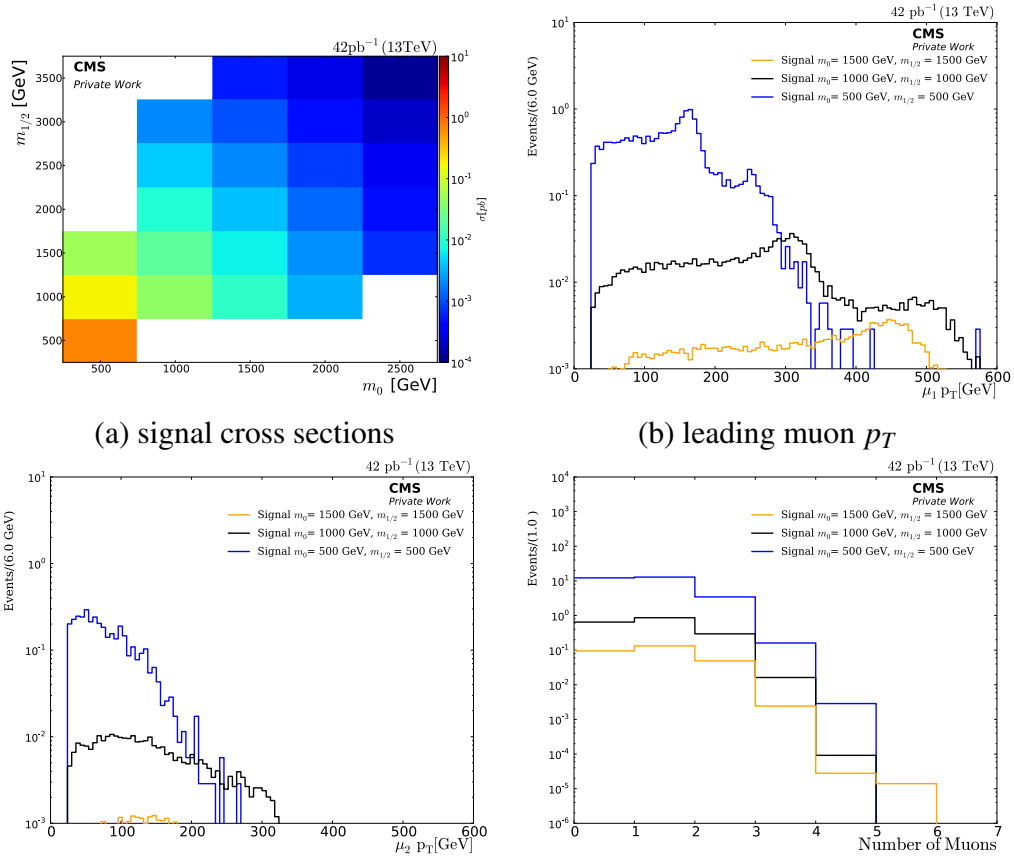

(a) signal cross sections

(b) leading muon p_T

(c) subleading muon p_T

(d) number of tight muons

Figure 3.1: Examples of the produced signal properties applying only the muon criteria from subsubsection 3.4.1. (a) shows the cross section of the produced signal points in the parameter space, (b) and (c) the leading and the subleading muon p_T and (d) the number of muons per event.

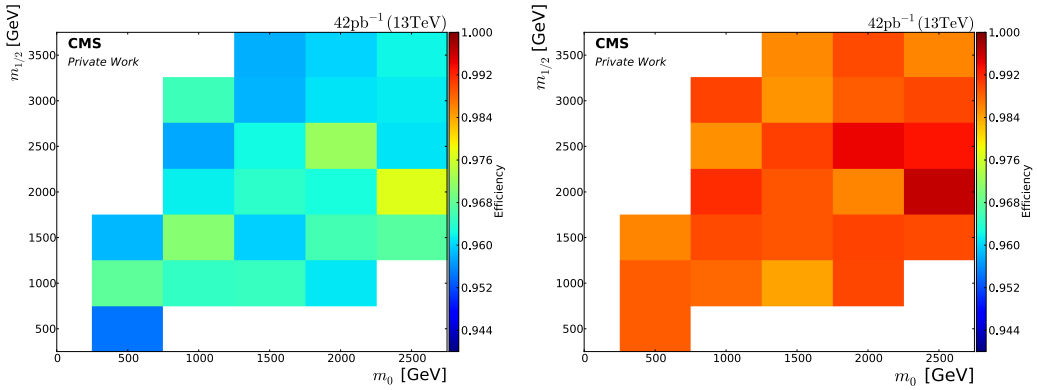

(a) Dimuon Trigger (μ_1 $p_T > 17$ GeV, μ_2 $p_T > 8$ GeV)

(b) Dimuon Trigger (μ_1 $p_T > 27$ GeV, μ_2 $p_T > 8$ GeV)

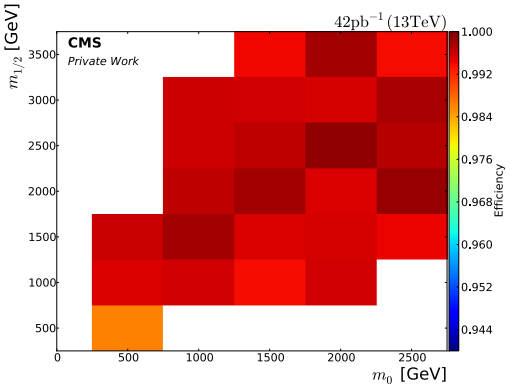

(c) Single Muon Trigger ($\mu\, p_T > 45$ GeV)

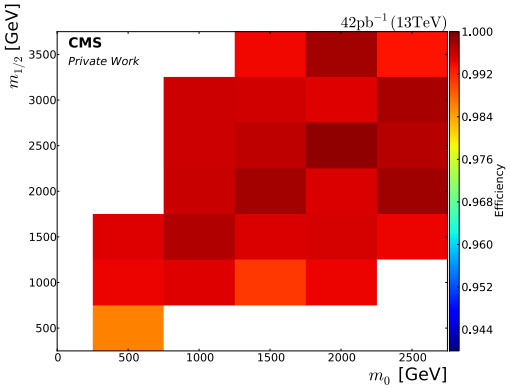

(d) Single Muon Trigger ($\mu\, p_T > 50$ GeV)

Figure 3.2: Efficiency for different samples and triggers.

3.3 Trigger

The events must fulfill multiple requirements. The first one is the trigger selection requirement. To select the most efficient trigger, a study was performed on simulation. For the produced samples, all requirements (muon criteria, jet criteria, invariant mass, b-jet veto and same sign, see subsection 3.4) have been applied except for the trigger selection. The analyzed triggers are:
Single Muon Trigger:

- HLT_Mu45_eta2p1
- HLT_Mu50

Dimuon Trigger:

- HLT_Mu27_TkMu8
- HLT_Mu17_TrkIsoVVL_TkMu8_TrkIsoVVL_DZ

To show the property of the compared trigger the ratio of the total numbers of events before and after applying the trigger for different samples can be seen in Figure 3.2 as a two dimensional plot of the parameter space for different triggers. Figure 3.3 shows a one dimensional plot for a selection of three signal points where (a) shows the only produced signal point where the efficiency of

the dimuon trigger is higher than the efficiency of the single muon trigger.

Even though that the threshold of the single muon triggers is higher than the threshold of the dimuon trigger the single muon triggers show a higher efficiency for the produced signal points, because of two chances instead of one chance to get triggered. Thus, the single muon triggers have been chosen.

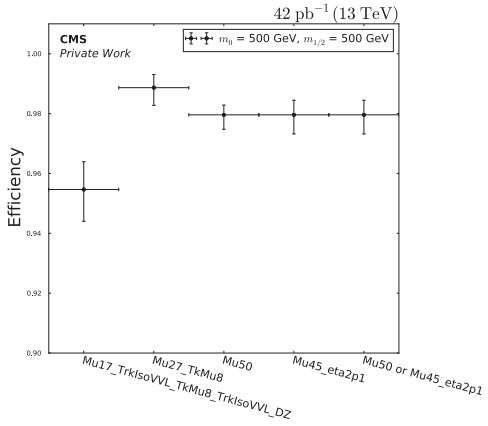

(a) $m_0 = 500\,\text{GeV}$, $m_{1/2} = 500\,\text{GeV}$

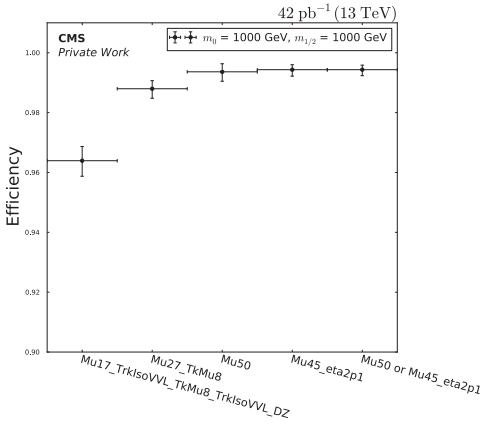

(b) $m_0 = 1000\,\text{GeV}$, $m_{1/2} = 1000\,\text{GeV}$

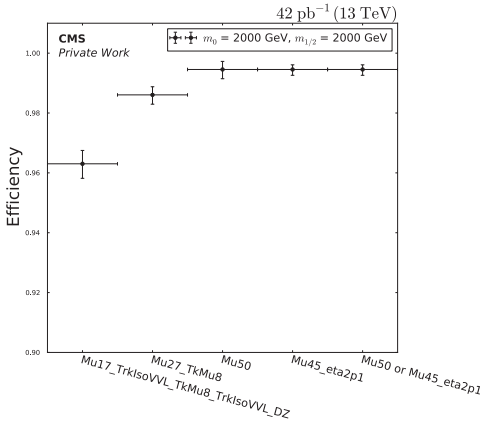

(c) $m_0 = 2000\,\text{GeV}$, $m_{1/2} = 2000\,\text{GeV}$

Figure 3.3: In this figure, the ratio between the number of events with and without a trigger after applying all selection criteria for three different signal points can be seen.

3.4 Selection Criteria

After the first selection with the trigger, additional selection criteria are applied. At first, the object selection ensures well reconstructed muons and jets events followed by signal based cuts that are used to extract the signal from the background distribution.

3.4.1 Object Selection

Muon Criteria

Due to the fact that the final state of the decay has two muons the event has to contain exactly two muons fulfilling the official Tight Muon ID [28]:

- **isGlobalMuon** : The reconstructed muon has to be tagged as Global-Muon. which means that they are reconstructed in the tracker and muon chambers[29].
- **isPFMuon** : The reconstructed muon has to be tagged as a Particle-flow muon.
- **NormalizedChi2 < 10** : The trajectory fit of the muons has to be good enough suppressing hadronic punch-through and muons from decays in flight.
- **numberOfValidMuonHits > 0** : At least one muon-chamber hit is required in the track fit suppressing hadronic punch-through and muons from decays in flight as well.
- **numberOfMatchedStations > 1** : Requires muon segments in at least two muon station suppressing punch-through and accidental track-to-segment matches.
- $|d_{xy}|$ **< 2 mm** : The transverse distance of the tracker track to the primary vertex has to be smaller than 2 mm. This suppresses cosmic muons and further suppresses muons from decays in flight.
- $|d_z|$ **< 5 mm** : The longitudinal distance of the tracker track to the primary vertex has to be smaller than 5 mm to suppress cosmic muons, muons from decays in flight and tracks from PU.
- **numberOfValidPixelHits > 0** : The number of hits in the pixel detector has to be one or higher which provides further suppression of muons from decays in flight.
- **trackerLayersWithMeasurement > 5** : A minimum of 6 tracker layers have to be hit which provides a good p_T measurement and suppresses muons from decays in flight.

In addition to the right muon ID, the threshold for the combined particle flow based muon isolation ([28]), using a cone size ΔR of 0.4, is set to 0.12

($\boldsymbol{I_{rel} < 0.12}$)[30]. In addition to the ID and isolation criteria a cut on the transverse momentum of the leading muon is applied at 55 GeV to suppress turn on effects of the triggers used and the transverse momentum of the subleading muon is set to at least 15 GeV. A visualization of the turn on effect of both single muon trigger can be seen in Figure 3.4, where the trigger efficiency of the HLT_Mu50 trigger as a function of the transverse momentum of the leading muon is shown. In this plot, the WJets background and only events with exactly one muon are choosen.

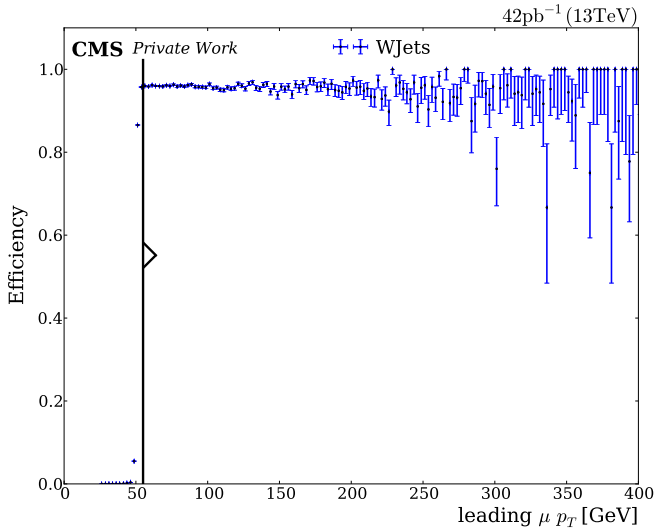

(a)

Figure 3.4: Turn on effect of the HLT_Mu50 single muon trigger using the WJets background sample and only events containing exactly one muon.

The effect of the muon selection criteria can be seen in Figure 3.5, showing a peak the the Z-boson mass (about 91 GeV) and mainly suppressing the QCD and the W + Jets background.

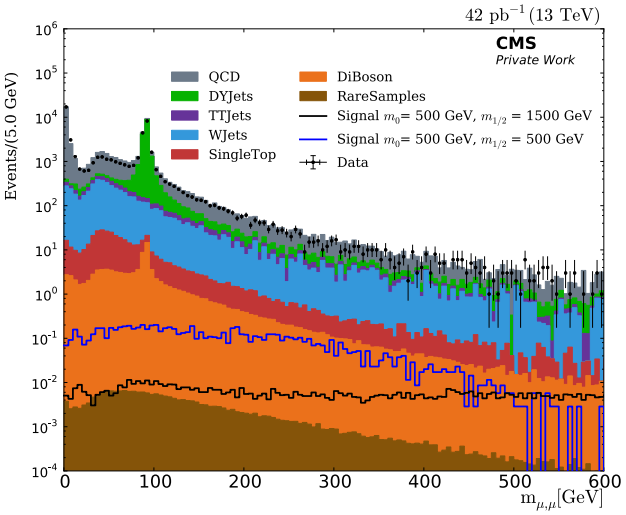

(a) invariant muon mass (before)

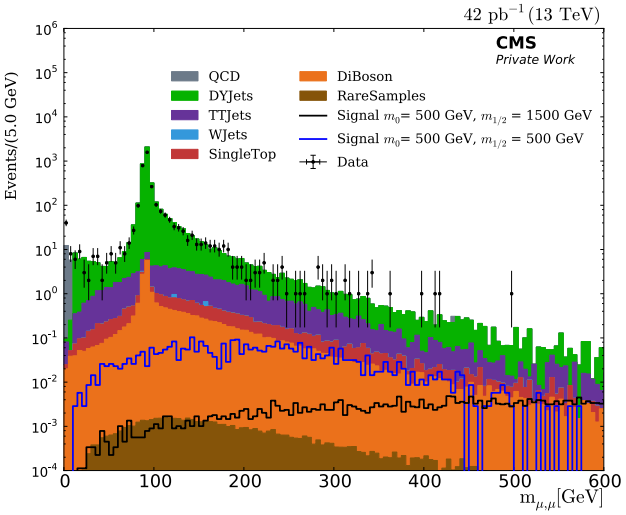

(b) invariant muon mass (after)

Figure 3.5: Comparison of the invariant mass of the two muons before (a) and after (b) applying the muon criteria. The effect of the selection is visible at the Z-boson peak (91 Gev).

Jet Criteria

The final state contains at least two light jets. As done with muons, official quality requirements are used and the event has to contain at least two jets. Each of the jets has to fulfil the Loose Jet Id[31]:

- **Pseudorapidity $|\eta| < 2.4$**:
- **Neutral Hadron Fraction < 0.99** : energy fraction of neutral particles in the hadron calorimeter has to be smaller than 0.99
- **Neutral EM Fraction < 0.99**: energy fraction of neutral particles in the electromagnetic calorimeter has to be smaller than 0.99
- **Number of Constituents > 1**: the number of particle components of the jet has to be higher than 1
- **Charged Hadron Fraction > 0**: energy fraction of charged particles in the hadron calorimeter has to be higher than 0
- **Charged Multiplicity > 0**: amount of charged jet components has to be higher than 0
- **Charged EM Fraction < 0.99**: energy fraction of charged particles in the electromagnetic calorimeter has to be smaller than 0.99

Additional to the Id requirements, only jets with a p_T higher than 30 GeV are used. The effect of the jet selection criteria can be seen in Figure 3.6.

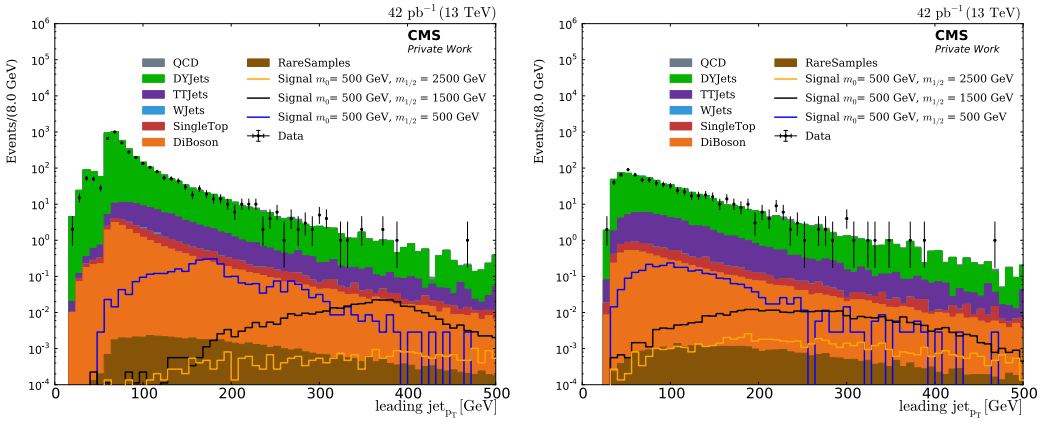

(a) (b)

Figure 3.6: Comparison of the transverse momentum of the leading jet before (a) and after (b) applying the jet selection criteria.

Invariant Mass

Only events where the invariant mass of the two muons is higher than 15 GeV are used to exclude events from J/ψ production or low mass Drell-Yan processes.

3.4.2 Signal Based Cuts

Missing Transverse Energy

The final state contains only a low amount of missing transverse energy. Therefore previous analysis[14] used this fact of low MET to separate signal, and thus only events with MET lower than 50 GeV were used. The MET plot (Figure 3.7(b))shows a shift between the background simulation and the taken data, due to known problems with the MET reconstruction in the used data sample. Therefore, the MET requirement was not used. This issue has been fixed in newer iterations and later reconstruction of the data.

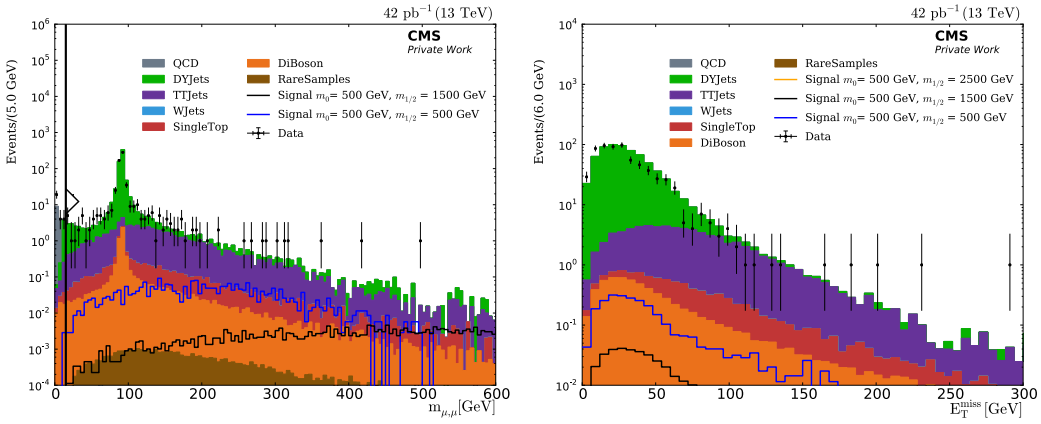

(a) (b)

Figure 3.7: (a) shows the invariant mass $m_{\mu\mu}$ after applying the muon and the jet selection criteria. The invariant mass criterion rejects all events with $m_{\mu\mu} < 15$ GeV.
The plot of the particle flow missing transverse energy (b) shows the shift between data and MC.

B-Jet Veto

The final state contains quarks from the first generation (up,down) only. If a jet is identified as a b-jet, the event has been rejected. The effect can be seen in Figure 3.8, showing the invariant mass of the two muons after the invariant mass cut (a) and after applying the b-jet veto (b). As one can see, the b-veto suppresses mainly the $t\bar{t}$ and the single-top background.

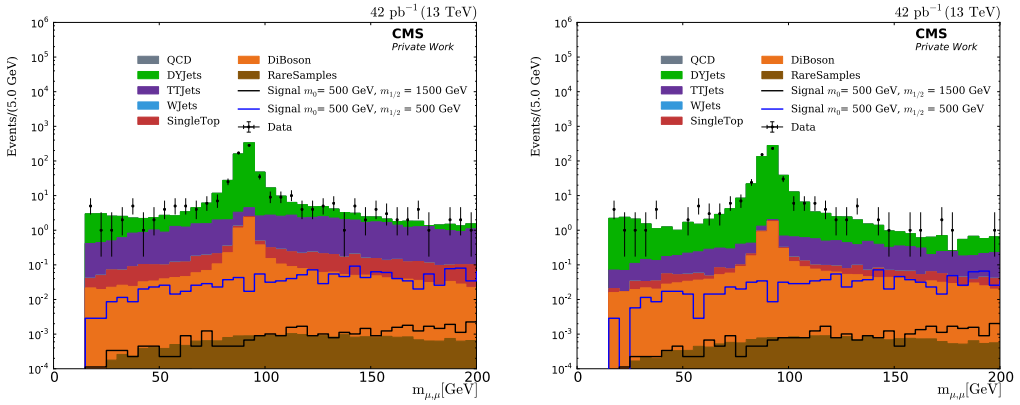

(a) before b-veto (b) after b-veto

Figure 3.8: Comparison with and without b-veto. Mainly the $t\bar{t}$- background is suppressed.

Same Sign

After the b-jet veto, the signal is still buried under the background. To gain a higher signal to background efficiency the last requirement takes into account that the charge of the two muons in the final state can be the same. Figure 3.9 shows the impact of this requirement to the invariant mass distribution of the two muons. The signal is well separated from the background distribution but the expected amount of SM background events are at the order of magnitude of $\mathcal{O}(10^{-1})$ and fulfilling this expectation, no data is left after this requirement. The contributing events in this distribution are from DiBoson, $t\bar{t}$, Single top and Rare sample processes. Overall, the expected number of events distributing from the Standard Model background is at $\mathcal{O}(10^{-1})$. Because of the low statistic, no data based estimation was done.

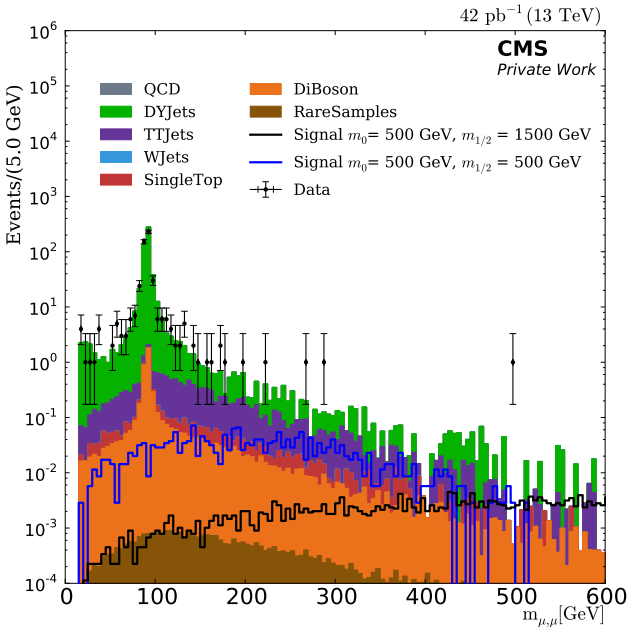

(a)

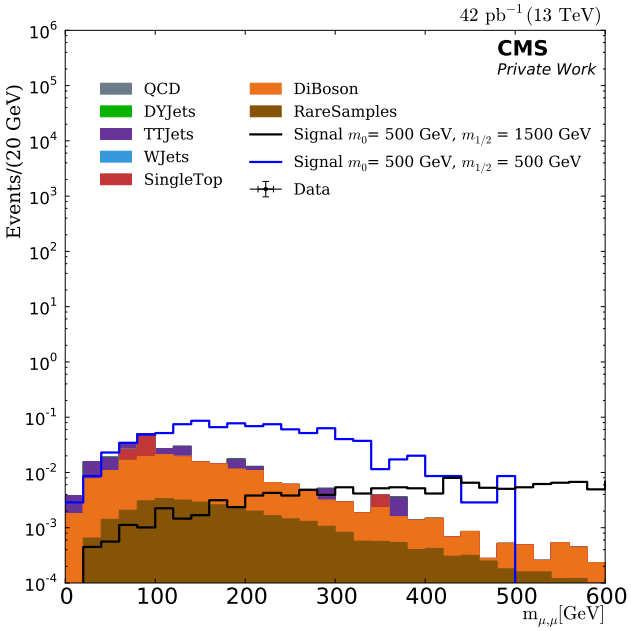

(b)

Figure 3.9: The same sign requirement of the two muons suppresses mainly Drell-Yan, $t\bar{t}$ and Di-Boson background. The expected number of events of the Standard Model background is reduced to the order of magnitude of 10^{-1}. Thus, no data is expected after this requirement.

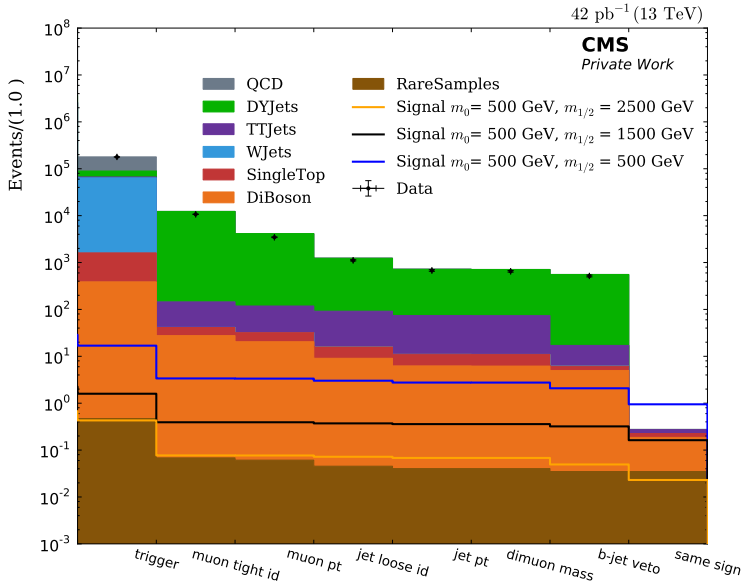

Figure 3.10: The cutflow shows the number of events after each applied requirement.

3.4.3 Summary

Figure 3.10 shows the effect of each applied requirement. The cut on the charge of the final muons has the highest impact on the background and the data. It reduces the number of background events from $\mathcal{O}(10^3)$ to $\mathcal{O}(10^{-1})$. The same sign charge requirement effects mostly the Drell-Yan and $t\bar{t}$ background. As expected from the order of magnitude of the background, no data fulfills the same sign charge requirement.
All requirement impacts can be seen in Table 3.3, where the cumulative percentage relative to the total number of events after the trigger requirement for each selection criteria is given. The first and the last column show the total number of events after the trigger requirement and after the same sign charge requirement.

Sample	N_{events}	Muon Criteria [%]	Jet Criteria [%]	$m_{\mu\mu}$ [%]	b-veto [%]	same charge [%]	$N_{events,end}$
Data	$1.7 \cdot 10^5$	1.94	0.38	0.36	0.29	0	0
Drell-Yan	$2.2 \cdot 10^4$	17.81	2.83	2.82	2.39	0	0
QCD	$8.9 \cdot 10^4$	0.02	0.01	$3.0 \cdot 10^{-4}$	0	0	0
$t\bar{t}$	$2.7 \cdot 10^3$	3.12	2.28	2.27	0.39	0.001	0.05
W	$6.1 \cdot 10^4$	0	0	0	0	0	0
Single top	$1.2 \cdot 10^3$	0.94	0.395	0.392	0.096	0.003	0.04
DiBoson	$3.8 \cdot 10^2$	5.28	1.60	1.59	1.28	0.039	0.15
Rare samples	$4.6 \cdot 10^{-2}$	12.96	8.56	8.56	7.42	7.41	0.03
m_0, $m_{1/2}$ [GeV]	N_{events}	Muon Criteria [%]	Jet Criteria [%]	$m_{\mu\mu}$ [%]	b-veto [%]	same charge [%]	$N_{events,end}$
500 , 500	16	19.83	16.36	16.34	12.36	5.63	0.94
1000, 1000	1.228	23.63	22.11	22.11	16.18	7.70	0.094
2000, 1500	0.063	24.47	23.80	23.80	16.73	7.61	0.005

Table 3.3: This table shows the impact of each cut on the background and some signal points. N_{events} shows the number of events after the trigger selection followed by the percentage of events surviving the named requirements. The total number of events after requiring every selection criteria $N_{events,end}$ can be seen in the last column.

3.5 Uncertainties

The uncertainties are divided into systematical and statistical uncertainties. The systematic uncertainties are taken from the 8 TeV analysis [14] but one has to take into account that the 8 TeV analysis uses a data driven method to calculate an estimation of non-promt contribution. Therefore, the uncertainties on the total yield, containing MC parts and data driven parts, have to be transformed back into MC only uncertainties:

$$\sigma_{13TeV} = \frac{\sigma_{8TeV} \cdot N_{8TeV,total}}{N_{8TeV,MC}} \tag{9}$$

In Equation 9, σ_{13TeV} is the uncertainty for the 13 TeV analysis, σ_{8TeV} the uncertainty from the 8 TeV analysis with the data-driven method, $N_{8TeV,total}$ the total number of events containing MC background and the fake estimation and $N_{8TeV,MC}$ the number of events without the fake estimation.

object specific uncertainties	background [%]	signal [%]
jet energy scale (JES)	3.7	7.8
jet energy resolution (JER)	0.6	2.6
μ momentum resolution	0.2	1.0
μ momentum scale	0.2	3.0
μ ID efficiency	1.2	1.4
b-tagging	0.6	1.4
general systematic uncertainties	background [%]	signal [%]
luminosity	4.6	4.6
PDF	6.0	5.0
cross sections	35.4	8.6
trigger efficiency	3.0	3.1

Table 3.4: Systematic uncertainties for 13 TeV calculated from the 8 TeV uncertainties except the luminosity uncertainty which is taken from [32]

The overall uncertainty on the background cross section was calculated by assigning an uncertainty of 50% on each single background cross section and summing up the uncertainties quadratically.

The statistical uncertainties are calculated from the total number of events in each bin using the poisson distribution. This leads to a statistical uncertainty of $\sigma_{stat} = \sqrt{N_{Events}}$. Because the background and signal samples are reweighted the statistic uncertainty is $\sigma_{stat} = \sqrt{N_{Events}} \cdot w$ where w is the reweight factor from Section 3.2.2.

4 Results

4.1 Final Distributions

After all requirements have been applied one can reconstruct the smuon and the gaugino mass. The final distributions can be seen in Figure 4.1. The mass of the smuon is reconstructed from the invariant mass of the leading and subleading muon and the two leading jets whereas the gaugino mass is reconstructed from the invariant mass of the subleading muon and the two leading jets (see subsubsection 1.2.3).

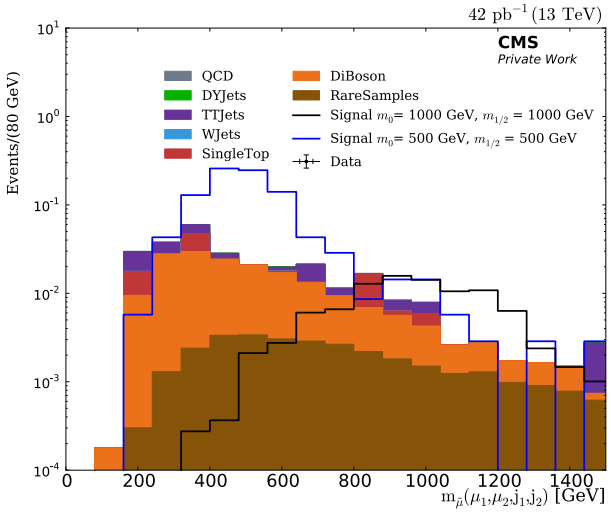

(a)

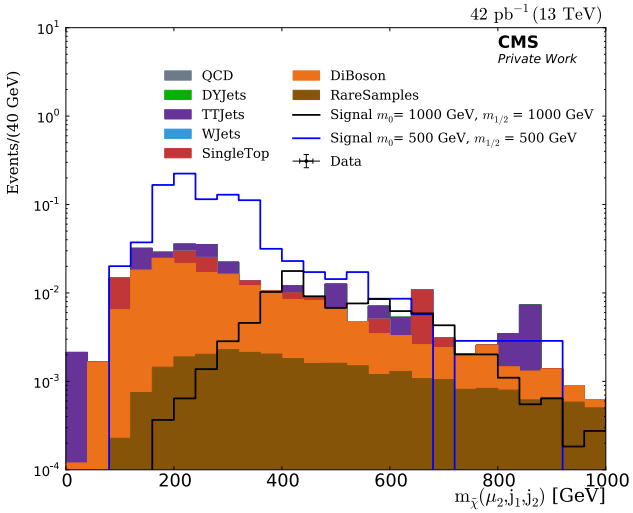

(b)

Figure 4.1: Reconstructed mass of the smuon and the gaugino. The smuon mass $m_{\tilde{\mu}}$ (a) is the invariant mass of both muons and the two leading jets whereas the gaugino mass $m_{\tilde{\chi}}$ (b) is the invariant mass of the subleading muon and two leading jets.

Figure 4.2 shows the transverse momentum of the leading and the subleading muon ((a), (b)) and the transverse momentum of the leading jet (c) after all requirements.

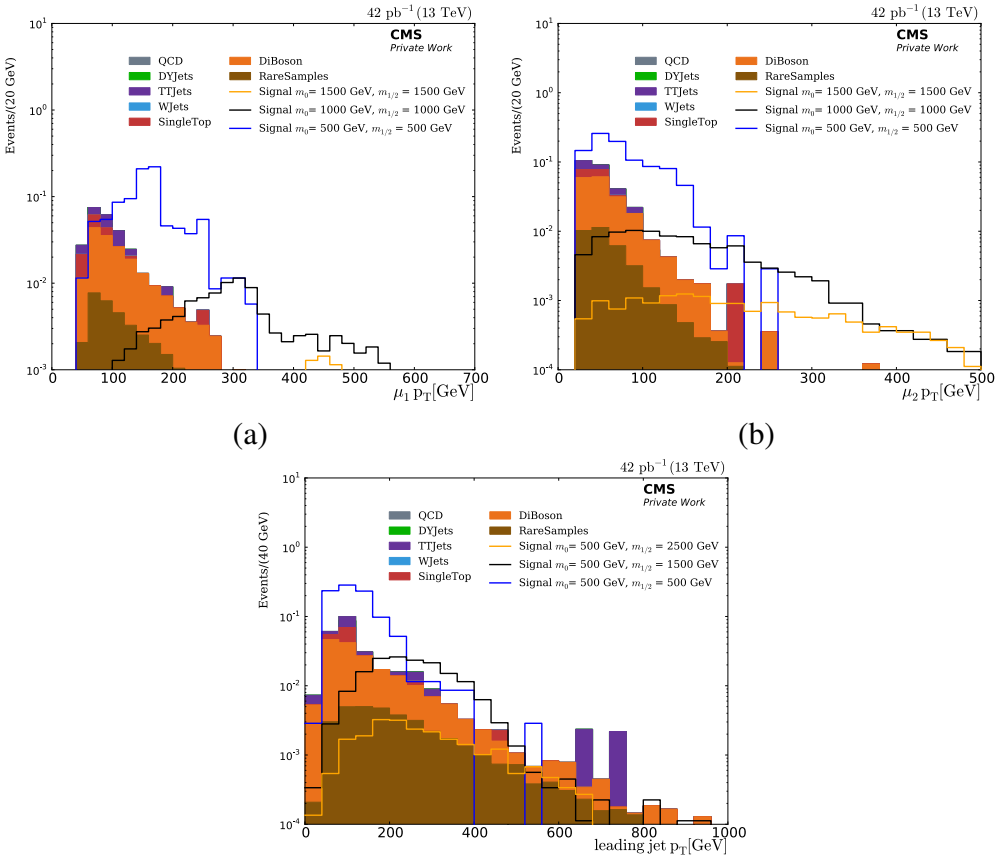

Figure 4.2: Transverse momentum of the leading (a) and the subleading muon (b) and the leading jet (c).

To improve the sensitivity of the analysis, the backgrounds are summed up and divided into six search regions. These search regions are differed by the value of the reconstructed smuon and gaugino mass in different intervalls. The expected background events as a function of the reconstructed smuon mass $m_{\tilde{\mu}}$ and the reconstructed gaugino mass $m_{\tilde{\chi}}$ divided into the six search regions can be found in Figure 4.3 in comparison to the contribution of one signal point ($m_0 = 500\,\text{GeV}$, $m_{1/2} = 1000\,\text{GeV}$). The borders of these regions can be found in Table 4.1 as well. For each of these search regions the total number of events from the background and the samples are calculated and can be seen in Figure 4.4 and Table 4.2.

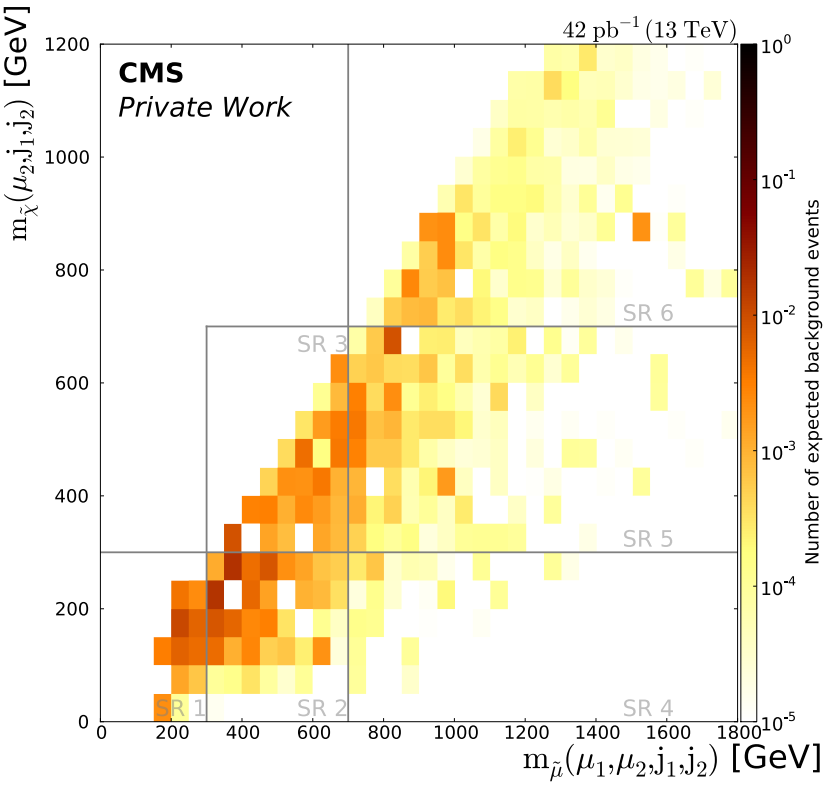

(a)

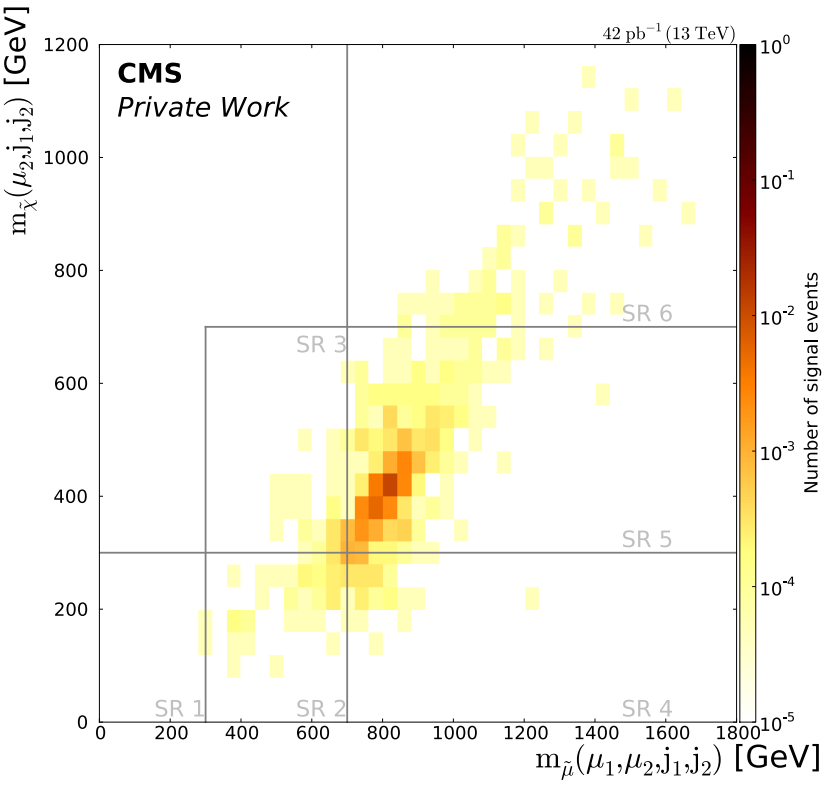

(b)

Figure 4.3: Distribution of the background (a) and one signal point($m_0 = 500\,\text{GeV}$, $m_{1/2} = 1000\,\text{GeV}$) (b) as a function of the reconstructed smuon mass $m_{\tilde{\mu}}$ and gaugino mass $m_{\tilde{\chi}}$ with visualized search regions.

Search Region	$m_{\tilde{\mu}}$ range	$m_{\tilde{\chi}}$ range
1	$m_{\tilde{\mu}} < 300$ GeV	$m_{\tilde{\chi}} < 300$ GeV
2	300 GeV $< m_{\tilde{\mu}} < 700$ GeV	$m_{\tilde{\chi}} < 300$ GeV
3	300 GeV $< m_{\tilde{\mu}} < 700$ GeV	300 GeV $< m_{\tilde{\chi}} < 700$ GeV
4	700 GeV $< m_{\tilde{\mu}}$	$m_{\tilde{\chi}} < 300$ GeV
5	700 GeV $< m_{\tilde{\mu}}$	300 GeV $< m_{\tilde{\chi}} < 700$ GeV
6	700 GeV $< m_{\tilde{\mu}}$	700 GeV $< m_{\tilde{\chi}}$

Table 4.1: Properties of the search regions.

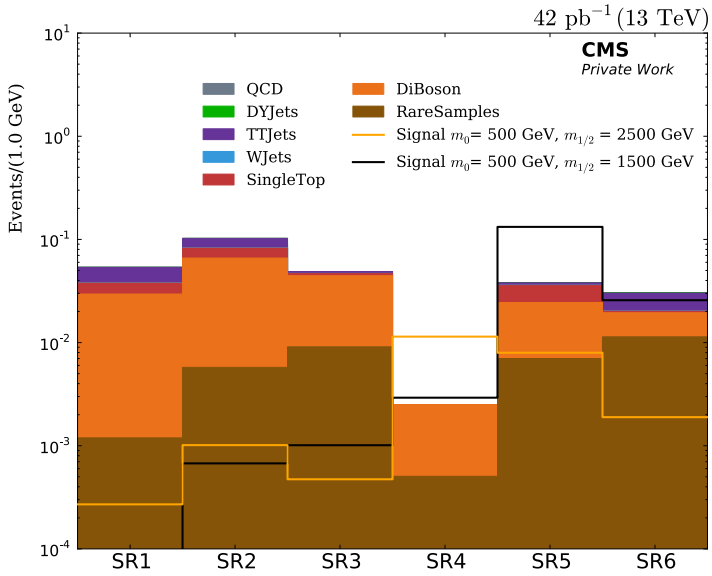

Figure 4.4: Total number of events of the different Standard Model backgrounds in each search region.

Process group	SR 1	SR 2	SR 3
$t\bar{t}$	$1.6 \cdot 10^{-2}$	$2.0 \cdot 10^{-2}$	$0.2 \cdot 10^{-2}$
SingleTop	$8.2 \cdot 10^{-3}$	$1.6 \cdot 10^{-2}$	$2.3 \cdot 10^{-3}$
DiBoson	$2.8 \cdot 10^{-2}$	$6.0 \cdot 10^{-2}$	$3.5 \cdot 10^{-2}$
Rare Sample	$1.2 \cdot 10^{-3}$	$5.8 \cdot 10^{-3}$	$9.1 \cdot 10^{-3}$
Process group	SR 4	SR 5	SR 6
$t\bar{t}$	0	$0.2 \cdot 10^{-2}$	$1.0 \cdot 10^{-2}$
SingleTop	0	$1.1 \cdot 10^{-2}$	$0.7 \cdot 10^{-3}$
DiBoson	$2.0 \cdot 10^{-3}$	$1.7 \cdot 10^{-2}$	$8.1 \cdot 10^{-3}$
Rare Sample	$0.5 \cdot 10^{-3}$	$7.0 \cdot 10^{-3}$	$1.1 \cdot 10^{-2}$

Table 4.2: Total number of events in each search region of the contributing Standard Model backgrounds.

5 Statistical Interpretation

5.1 Limit Setting

As there is no data left in the final distributions and therefore no excess has been seen upper limits on the signal cross section have been calculated and then converted into limits on the λ'_{211} coupling. To calculate those limits the HiggsCombine [33] tool is used. This tool then provides CL_s limits which are described in the next section.

5.1.1 CLs

As mentioned before, to calculate the upper limits the modified frequentist method or CL_s method is used. This section is based on [34].
At first one defines a hypothesis test with two hypotheses. A null hypothesis with only the Standard Model background and an alternate hypothesis which contains the signal and the background.

A test-statistic Q is constructed and the confidence in the alternate hypothesis (signal + background) is then given by :

$$CL_{s+b} = P_{s+b}(Q \leq Q_{obs}) \tag{10}$$

with

$$P_{s+b}(Q \leq Q_{obs}) = \int_{-\infty}^{Q_{obs}} \frac{dP_{s+b}}{dQ} dQ \tag{11}$$

($\frac{dP_{s+b}}{dQ}$ = probability distribution function of the test statistic for signal + background) The confidence in the null hypothesis is given by:

$$CL_b = P_B(Q \leq Q_{obs}) \tag{12}$$

with

$$P_b(Q \leq Q_{obs}) = \int_{-\infty}^{Q_{obs}} \frac{dP_b}{dQ} dQ \tag{13}$$

Using these definitions the CL_s is then defined as:

$$CL_s \equiv \frac{CL_{s+b}}{CL_b} \tag{14}$$

The alternate hypothesis is then considered excluded at the confidence level CL when $1 - CL_s \leq CL$. The exclusion limits are set at the 95 % confidence level and as test statistic the profile likelihood is used [35].

5.1.2 Results

With the CL_s method described before, limits have been calculated for all signal points. To estimate the behavior of the upper limit an extrapolation to higher luminosities has been done, using only expected limits. The HiggsCombine tool provides upper limits on the crosssection σ which can be found in the appendix. This upper limit can be converted into an upper limit on the coupling by taking into account that the cross section scales with the coupling quadratically, $\sigma \propto {\lambda'_{211}}^2$.
Therefore (with $\lambda'_{211,signal} = 0.01$):

$$\frac{\sigma_{limit}}{\sigma_{signal}} = \frac{{\lambda'_{211,limit}}^2}{{\lambda'_{211,signal}}^2} \Rightarrow \lambda'_{211,limit} = \lambda'_{211,signal} \cdot \sqrt{\frac{\sigma_{limit}}{\sigma_{signal}}} \tag{15}$$

Figure 5.1 shows the impact of higher luminosity on the expected upper limit. The expected upper limit on λ'_{211} is shown as a function of m_0 and $m_{1/2}$ with different luminosities. One can see that the limit on the λ'_{211} coupling improves for higher luminosities.

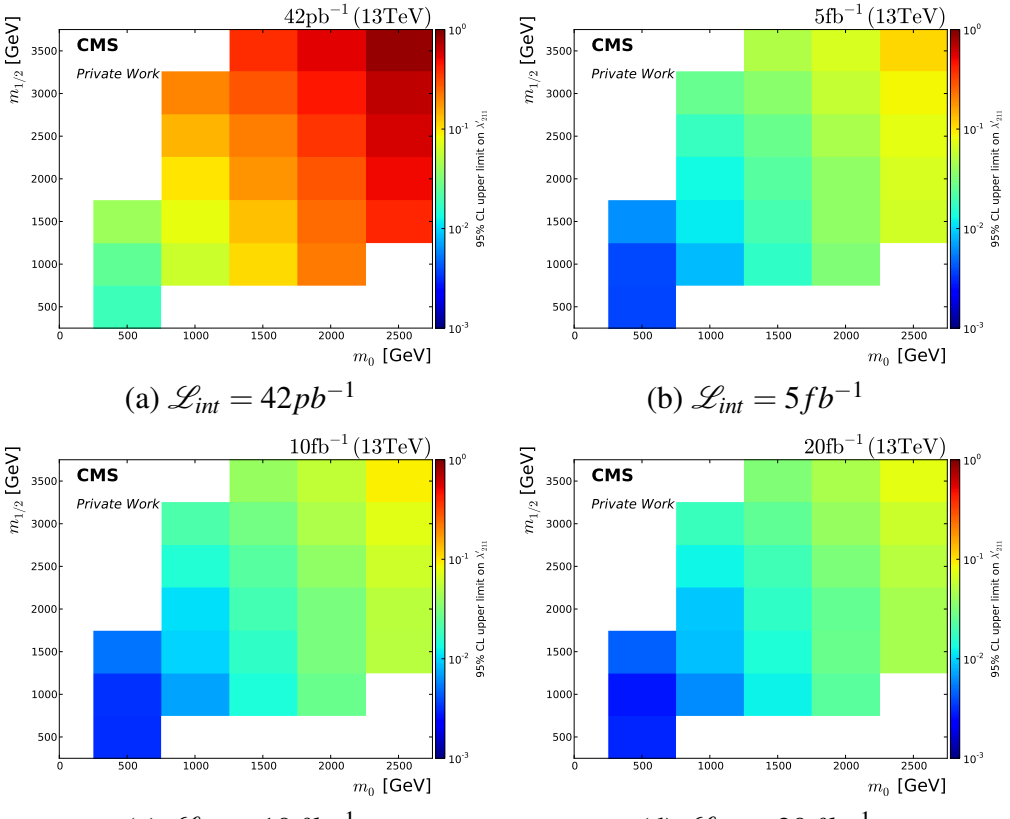

(a) $\mathscr{L}_{int} = 42pb^{-1}$ (b) $\mathscr{L}_{int} = 5fb^{-1}$

(c) $\mathscr{L}_{int} = 10fb^{-1}$ (d) $\mathscr{L}_{int} = 20fb^{-1}$

Figure 5.1: Expected upper limits for different luminosities with all signal points included. One can see that the upper limit improves with each step to higher luminosity.

Another visualization of the two dimensional plot from Figure 5.1 can be seen in Figure 5.2. By fixing the mass $m_{1/2}$ one gets an one dimensional representation of the upper limits.

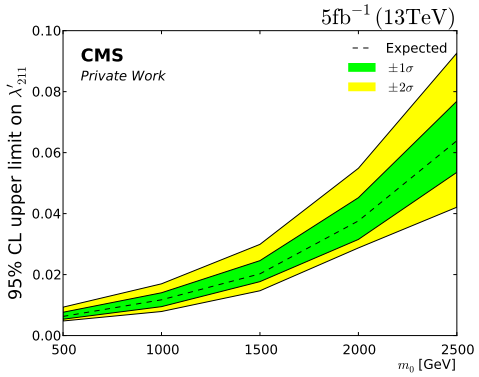

(a) $\mathscr{L}_{int} = 5fb^{-1}$, $m_{1/2} = 1500GeV$

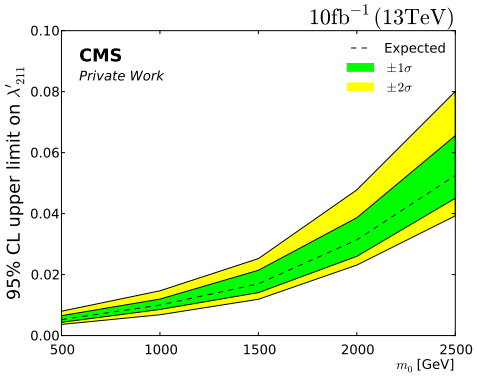

(b) $\mathscr{L}_{int} = 10fb^{-1}$, $m_{1/2} = 1500GeV$

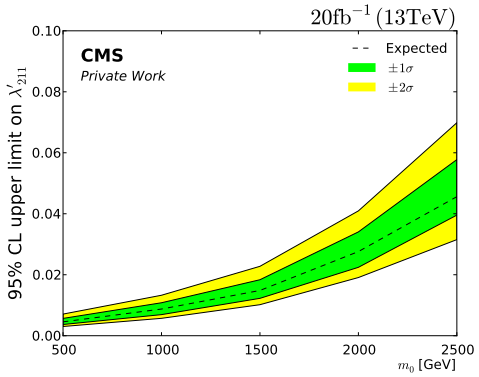

(c) $\mathscr{L}_{int} = 20fb^{-1}$, $m_{1/2} = 1500GeV$

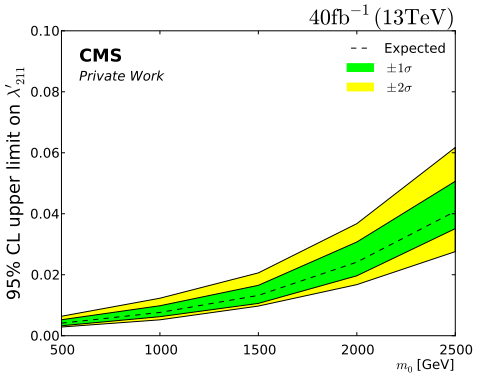

(d) $\mathscr{L}_{int} = 40fb^{-1}$, $m_{1/2} = 1500GeV$

Figure 5.2: Expected upper limits for different luminosities with fixed $m_{1/2}$ at 1500 GeV for $\mathscr{L}$ = 5 fb^{-1}, 10 fb^{-1}, 20 fb^{-1} and 40 fb^{-1}.

5.1.3 Comparison to 8 TeV

To verify the calculated limits and to make an outlook on what integrated luminosity could be needed to gain a comparable significance to older analysis a comparison with the upper limits from the 8 TeV analysis has been done and can be seen in Table 5.1. The difference between the two is that the 8 TeV analysis uses next to leading order cross sections whereas this analysis uses leading order cross sections.

m_0, $m_{1/2}$ [GeV]	$\mathscr{L}_{int}$ [fb^{-1}]	coupling limit λ'_{211} (8 TeV)	coupling limit λ'_{211} (13 TeV)
500 , 500	19.7	0.0031(obs.)	
	0.042		0.0189(obs.)
	5		0.0038(exp.)
	10		0.0032(exp.)
	15		0.0031(exp.)
	20		0.0030(exp.)
	40		0.0027(exp.)
1000 , 1000	19.7	0.0071(obs.)	
	0.042		0.0611(obs.)
	5		0.0086(exp.)
	10		0.0072(exp.)
	15		0.0066(exp.)
	20		0.0062(exp.)
	40		0.0056(exp.)
1500 , 1500	19.7	0.0290(obs.)	
	0.042		0.1287(obs.)
	5		0.0202(exp.)
	10		0.0170(exp.)
	15		0.0157(exp.)
	20		0.0148(exp.)
	40		0.0132(exp.)

Table 5.1: Comparison between the upper limits for 8 TeV and for 13 TeV. The 8 TeV limits are taken from [14] and [36].

As shown in Table 5.1, the limit on λ'_{211} depends on the set of parameters m_0, $m_{1/2}$ as well as on the luminosity. For higher universal masses, the limit rises. For higher luminosities, the limit improves but not as much as expected compared to the 8 TeV analysis due to the systematic uncertainties and the not negligible number of background events. The luminosity of 5 fb^{-1} leads to an upper limit on the coupling of the same order of magnitude as the limit provided from the 8 TeV analysis.

6 Conclusion and Outlook

In this analysis, an investigation of an R-parity violating production and decay of a SUSY smuon into two muons and jets has been done. The event selection criteria and their impact on the used data, background and signal samples are presented and the uncertainties were calculated using a previous analysis.
The analysis shows good agreement of the taken data and the simulation before the final same sign requirement, even with low statistics and the known MET reconstruction problem. Afterwards, no data event was left and therefore only exclusion limits are presented. The calculation of limits was done with the CLs method and those limits on the cross section are converted into limits on the coupling λ'_{211}. Thus, it was possible to set first limits for 13 TeV. Those limits have been extrapolated to higher luminosities and have been compared with limits from the 8 TeV analysis.
This comparison leads to the conclusion that an integrated luminosity $\mathscr{L}_{int}$ of 5 fb^{-1} would provide an expected upper limit on the coupling λ'_{211} with the same order of magnitude as in the 8 TeV analysis.

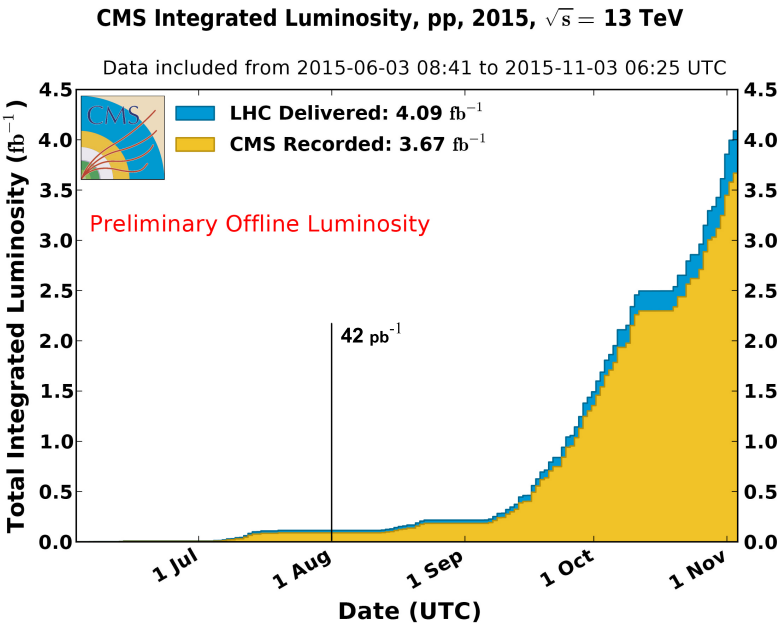

Figure 6.1: Total Integrated Luminosity in 2015 from CMS by day. (taken from [37])

As shown in Figure 6.1, the integrated luminosity has reached $\mathscr{L}_{int} = 3.67\text{fb}^{-1}$ at the end of the 2015 data taking period. Therefore, one can expect a high enough integrated luminosity for a upper limit on λ'_{211} with the same order of magnitude as with 8 TeV in 2016. This leads to a higher amount of statistic in data and allows to perform a data driven estimation comparable to the 8 TeV analysis which will raise the precision of this analysis.

7 Appendix

Monte Carlo Samples	N_{Events}
DYJetsToLL_M-10to50_TuneCUETP8M1_13TeV-amcatnloFXFX-pythia8/RunIISpring15DR74-Asympt25ns_MCRUN2_74_V9-v1/MINIAODSIM	30535559
DYJetsToLL_M-50_TuneCUETP8M1_13TeV-amcatnloFXFX-pythia8/RunIISpring15DR74-Asympt25ns_MCRUN2_74_V9-v3/MINIAODSIM	28825132
QCD_Pt-15to20_MuEnrichedPt5_TuneCUETP8M1_13TeV_pythia8/RunIISpring15MiniAODv2-74X_mcRun2_asymptotic_v2-v1/MINIAODSIM	2359418
QCD_Pt-20to30_MuEnrichedPt5_TuneCUETP8M1_13TeV_pythia8/RunIISpring15MiniAODv2-74X_mcRun2_asymptotic_v2-v1/MINIAODSIM	2292361
/QCD_Pt-30to50_MuEnrichedPt5_TuneCUETP8M1_13TeV_pythia8/RunIISpring15DR74-Asympt25ns_MCRUN2_74_V9-v1/MINIAODSIM	4941786
QCD_Pt-50to80_MuEnrichedPt5_TuneCUETP8M1_13TeV_pythia8/RunIISpring15DR74-Asympt25ns_MCRUN2_74_V9-v1/MINIAODSIM	5003055
QCD_Pt-80to120_MuEnrichedPt5_TuneCUETP8M1_13TeV_pythia8/RunIISpring15DR74-Asympt25ns_MCRUN2_74_V9-v1/MINIAODSIM	3681268
QCD_Pt-120to170_MuEnrichedPt5_TuneCUETP8M1_13TeV_pythia8/RunIISpring15DR74-Asympt25ns_MCRUN2_74_V9-v2/MINIAODSIM	4026104
QCD_Pt-170to300_MuEnrichedPt5_TuneCUETP8M1_13TeV_pythia8/RunIISpring15DR74-Asympt25ns_MCRUN2_74_V9-v2/MINIAODSIM	2451095
QCD_Pt-300to470_MuEnrichedPt5_TuneCUETP8M1_13TeV_pythia8/RunIISpring15DR74-Asympt25ns_MCRUN2_74_V9-v2/MINIAODSIM	1391609
QCD_Pt-470to600_MuEnrichedPt5_TuneCUETP8M1_13TeV_pythia8/RunIISpring15DR74-Asympt25ns_MCRUN2_74_V9-v2/MINIAODSIM	1878616
QCD_Pt-600to800_MuEnrichedPt5_TuneCUETP8M1_13TeV_pythia8/RunIISpring15DR74-Asympt25ns_MCRUN2_74_V9-v2/MINIAODSIM	1983363
QCD_Pt-800to1000_MuEnrichedPt5_TuneCUETP8M1_13TeV_pythia8/RunIISpring15DR74-Asympt25ns_MCRUN2_74_V9-v2/MINIAODSIM	1231585
QCD_Pt-1000toInf_MuEnrichedPt5_TuneCUETP8M1_13TeV_pythia8/RunIISpring15DR74-Asympt25ns_MCRUN2_74_V9-v2/MINIAODSIM	1906355
TTJets_TuneCUETP8M1_13TeV-amcatnloFXFX-pythia8/RunIISpring15DR74-Asympt25ns_MCRUN2_74_V9-v1/MINIAODSIM	42408530
WJetsToLNu_TuneCUETP8M1_13TeV-amcatnloFXFX-pythia8/RunIISpring15DR74-Asympt25ns_MCRUN2_74_V9-v1/MINIAODSIM	24151270

Table 7.1: monte carlo samples

Monte Carlo Samples	N_{Events}
WWTo2L2Nu_13TeV-powheg/RunIISpring15DR74-Asympt25ns_MCRUN2_74_V9-v1/MINIAODSIM	1930000
WWTo4Q_13TeV-powheg/RunIISpring15DR74-Asympt25ns_MCRUN2_74_V9-v3/MINIAODSIM	1995200
ZZTo2L2Q_13TeV_amcatnloFXFX_madspin_pythia8/RunIISpring15DR74-Asympt25ns_MCRUN2_74_V9-v1/MINIAODSIM	18898680
ZZTo4L_13TeV-amcatnloFXFX-pythia8/RunIISpring15DR74-Asympt25nsRaw_MCRUN2_74_V9-v1/MINIAODSIM	10420567
WZTo1L1Nu2Q_13TeV_amcatnloFXFX_madspin_pythia8/RunIISpring15DR74-Asympt25ns_MCRUN2_74_V9-v1/MINIAODSIM	24661367
ZZTo2Q2Nu_13TeV_amcatnloFXFX_madspin_pythia8/RunIISpring15DR74-Asympt25ns_MCRUN2_74_V9-v1/MINIAODSIM	35124970
WW_DoubleScattering_13TeV-pythia8/RunIISpring15DR74-Asympt25ns_MCRUN2_74_V9-v1/MINIAODSIM	843514
WZTo3LNu_TuneCUETP8M1_13TeV-powheg-pythia8/RunIISpring15DR74-Asympt25ns_MCRUN2_74_V9-v1/MINIAODSIM	1925000
WWToLNuQQ_13TeV-powheg/RunIISpring15DR74-Asympt25ns_MCRUN2_74_V9-v1/MINIAODSIM	1969600
ST_tW_top_5f_inclusiveDecays_13TeV-powheg-pythia8_TuneCUETP8M1/RunIISpring15DR74-Asympt25ns_MCRUN2_74_V9-v1/MINIAODSIM	995600
ST_s-channel_4f_leptonDecays_13TeV-amcatnlo-pythia8_TuneCUETP8M1/RunIISpring15DR74-Asympt25ns_MCRUN2_74_V9-v1/MINIAODSIM	984400
ST_t-channel_5f_leptonDecays_13TeV-amcatnlo-pythia8_TuneCUETP8M1/RunIISpring15DR74-Asympt25ns_MCRUN2_74_V9-v1/MINIAODSIM	2966200
ST_tW_antitop_5f_inclusiveDecays_13TeV-powheg-pythia8_TuneCUETP8M1/RunIISpring15DR74-Asympt25ns_MCRUN2_74_V9-v1/MINIAODSIM	1000000
WpWpJJ_QCD_TuneCUETP8M1_13TeV-madgraph-pythia8/RunIISpring15DR74-Asympt25ns_MCRUN2_74_V9-v1/MINIAODSIM	150000
WpWpJJ_EWK_TuneCUETP8M1_13TeV-madgraph-pythia8/RunIISpring15DR74-Asympt25ns_MCRUN2_74_V9-v1/MINIAODSIM	150000

Table 7.2: monte carlo samples

m_0, $m_{1/2}$ [GeV]	cross section [fb]	N_{Events}	m_0, $m_{1/2}$ [GeV]	cross section [fb]	N_{Events}
500, 500	675.616	10000	1500, 3500	0.561	20000
500, 1000	177.003	20000	2000, 1000	3.071	20000
500, 1500	52.916	20000	2000, 1500	2.133	20000
1000, 1000	42.9	20000	2000, 2000	1.385	20000
1000, 1500	20.252	20000	2000, 2500	0.851	20000
1000, 2000	9.106	20000	2000, 3000	0.499	20000
1000, 2500	4.248	20000	2000, 3500	0.282	20000
1000, 3000	2.013	20000	2500, 1500	0.712	20000
1500, 1000	10.772	20000	2500, 2000	0.501	20000
1500, 1500	6.570	20000	2500, 2500	0.334	20000
1500, 2000	3.733	20000	2500, 3000	0.213	20000
1500, 2500	2.008	20000	2500, 3500	0.130	20000
1500, 3000	1.060	20000			

Table 7.3: signal points produced

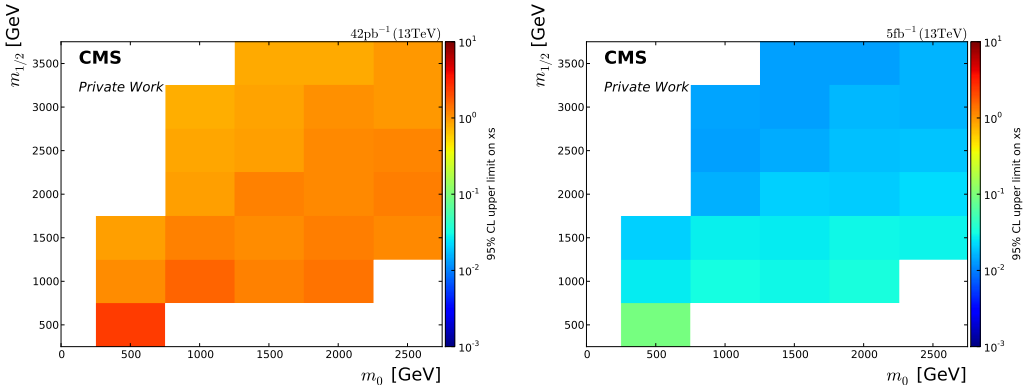

(a) $\mathscr{L}_{int} = 42pb^{-1}$

(b) $\mathscr{L}_{int} = 5fb^{-1}$

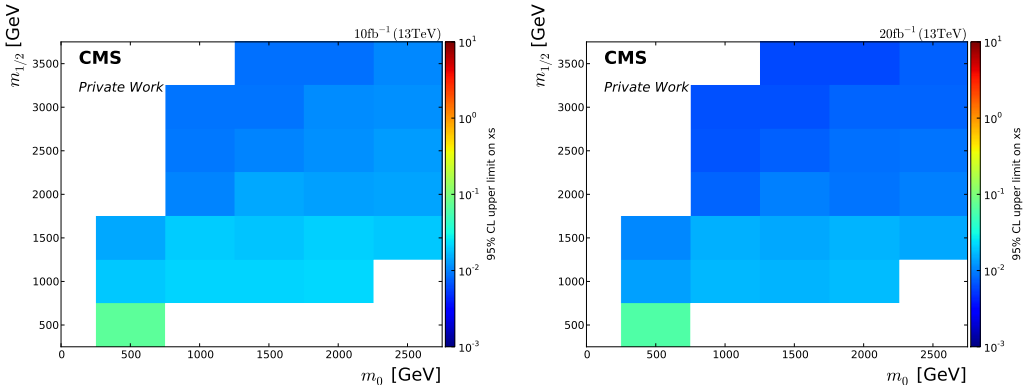

(c) $\mathscr{L}_{int} = 10fb^{-1}$

(d) $\mathscr{L}_{int} = 20fb^{-1}$

Figure 7.1: Expected upper cross section limits for different luminosities with all signal points included.

m_0, $m_{1/2}$ [GeV]	cross section [pb]	$\mathscr{L}_{int}$ [fb^{-1}]	upper cross section limit [pb] (13 TeV)
500 , 500	0.6756	0.042	0.6222
		5	0.0960
		10	0.0713
		15	0.0674
		20	0.0623
		40	0.0506
1000 , 1000	0.0429	0.042	1.6033
		5	0.0317
		10	0.0220
		15	0.0187
		20	0.0168
		40	0.0132
1500 , 1500	0.0066	0.042	1.0884
		5	0.0269
		10	0.0189
		15	0.0162
		20	0.0145
		40	0.0115

Table 7.4: Cross section limits for different luminosities.

References

[1] GRIFFITHS, D. J. *Introduction to elementary particles*. 2., rev. ed., 5. reprint. Physics textbook. Wiley-VCH, Weinheim, 2011. 454 pp. ISBN: 978-3-527-40601-2.

[2] FUKUDA, Y., ET AL. Evidence for Oscillation of Atmospheric Neutrinos. *Physical Review Letters* 81, 8 (Aug. 24, 1998), 1562–1567. ISSN: 0031-9007, 1079-7114. DOI: 10.1103/PhysRevLett.81.1562. URL: http://link.aps.org/doi/10.1103/PhysRevLett.81.1562 (visited on 11/09/2015).

[3] AHMAD, Q. R., ET AL. Measurement of the Rate of ν e + d $\rightarrow$ p + p + e Interactions Produced by B 8 Solar Neutrinos at the Sudbury Neutrino Observatory. *Physical Review Letters* 87, 7 (July 25, 2001). ISSN: 0031-9007, 1079-7114. DOI: 10.1103/PhysRevLett.87.071301. URL: http://link.aps.org/doi/10.1103/PhysRevLett.87.071301 (visited on 11/09/2015).

[4] AHMAD, Q. R., ET AL. Direct Evidence for Neutrino Flavor Transformation from Neutral-Current Interactions in the Sudbury Neutrino Observatory. *Physical Review Letters* 89, 1 (June 13, 2002). ISSN: 0031-9007, 1079-7114. DOI: 10.1103/PhysRevLett.89.011301. URL: http://link.aps.org/doi/10.1103/PhysRevLett.89.011301 (visited on 11/09/2015).

[5] *The Nobel Prize in Physics 2015*. URL: https://www.nobelprize.org/nobel_prizes/physics/laureates/2015/ (visited on 11/09/2015).

[6] AAIJ, R., ET AL. Observation of J / Ψ p Resonances Consistent with Pentaquark States in Λ b 0 $\rightarrow$ J / Ψ K - p Decays. *Physical Review Letters* 115, 7 (Aug. 12, 2015). ISSN: 0031-9007, 1079-7114. DOI: 10.1103/PhysRevLett.115.072001. URL: http://link.aps.org/doi/10.1103/PhysRevLett.115.072001.

[7] DAWSON, S. Introduction to electroweak symmetry breaking. In: *High energy physics and cosmology. Proceedings, Summer School, Trieste, Italy, June 29-July 17, 1998*. 1998, 1–83. arXiv: hep-ph/9901280 [hep-ph]. URL: http://alice.cern.ch/format/showfull?sysnb=0301862.

[8] CHATRCHYAN, S., ET AL. Observation of a new boson at a mass of 125 GeV with the CMS experiment at the LHC. *Physics Letters B* 716, 1 (Sept. 2012), 30–61. ISSN: 03702693. DOI: 10.1016/j.physletb.2012.08.021. URL: http://linkinghub.elsevier.com/retrieve/pii/S0370269312008581.

[9] AAD, G., ET AL. Observation of a new particle in the search for the Standard Model Higgs boson with the ATLAS detector at the LHC. *Physics Letters B* 716, 1 (Sept. 2012), 1–29. DOI: 10.1016/j.physletb.2012.08.020. URL: http://linkinghub.elsevier.com/retrieve/pii/S037026931200857X (visited on 12/10/2015).

[10] BERTONE, G., HOOPER, D., AND SILK, J. Particle dark matter: evidence, candidates and constraints. *Physics Reports* 405, 5 (Jan. 2005), 279–390. ISSN: 03701573. DOI: 10.1016/j.physrep.2004.08.031. URL: http://linkinghub.elsevier.com/retrieve/pii/S0370157304003515 (visited on 10/17/2015).

[11] MARTIN, S. P. A Supersymmetry primer (2011). arXiv: hep-ph/9709356 [hep-ph].

[12] BARBIER, R., ET AL. R-Parity-violating supersymmetry. *Physics Reports* 420, 1 (Nov. 2005), 1–195. ISSN: 03701573. DOI: 10.1016/j.physrep.2005.08.006. URL: http://linkinghub.elsevier.com/retrieve/pii/S0370157305003327 (visited on 10/26/2015).

[13] DREINER, H. K., ET AL. Baryon triality and neutrino masses from an anomalous flavor. *Nuclear Physics B* 774, 1 (July 2007), 127–167. ISSN: 05503213. DOI: 10.1016/j.nuclphysb.2007.03.028. URL: http://linkinghub.elsevier.com/retrieve/pii/S0550321307002386 (visited on 10/26/2015).

[14] *Search for R-parity violating supersymmetry in dilepton channels*. Tech. rep. CMS-PAS-SUS-14-018. Geneva: CERN, 2015. URL: http://cds.cern.ch/record/2059845.

[15] EVANS, L., AND BRYANT, P. LHC Machine. *Journal of Instrumentation* 3, 8 (Aug. 14, 2008), S08001–S08001. ISSN: 1748-0221. DOI: 10.1088/1748-0221/3/08/S08001. URL: http://stacks.iop.org/1748-0221/3/i=08/a=S08001?key=crossref.c8f0bc7a1a7c3a99bae6dd73f234f91b (visited on 10/19/2015).

[16] *CMS Public | CMS Experiment*. URL: http://cms.web.cern.ch/ (visited on 11/08/2015).

[17] COMMUNICATION GROUP *CERN faq, LHC the guide*. Feb. 2009. URL: http://cds.cern.ch/record/1165534/files/CERN-Brochure-2009-003-Eng.pdf.

[18] *CMS detector design | CMS Experiment*. URL: http://cms.web.cern.ch/news/cms-detector-design (visited on 10/19/2015).

[19] THE CMS COLLABORATION, ET AL. The CMS experiment at the CERN LHC. *Journal of Instrumentation* 3, 8 (Aug. 14, 2008), S08004–S08004. ISSN: 1748-0221. DOI: 10.1088/1748-0221/3/08/S08004. URL: http://stacks.iop.org/1748-0221/3/i=08/a=S08004?key=crossref.fc7f4422618a075830e017d1d930a35c (visited on 10/19/2015).

[20] *CMS-doc-5581-v1: CMS slice raw illustrator files*. URL: https://cms-docdb.cern.ch/cgi-bin/PublicDocDB/ShowDocument?docid=5581 (visited on 11/06/2015).

[21] THE CMS COLLABORATION *Particle-Flow Event Reconstruction in CMS and Performance for Jets, Taus, and MET*. Tech. rep. CMS-PAS-PFT-09-001. 2009. Geneva: CERN, Apr. 2009. URL: http://cds.cern.ch/record/1194487.

[22] *III Physikalisches Institut A · GitHub*. URL: https://github.com/Aachen-3A (visited on 10/21/2015).

[23] *matplotlib: python plotting — Matplotlib 1.4.3 documentation*. URL: http://matplotlib.org/ (visited on 10/21/2015).

[24] *BRIL Work Suite*. URL: http://cms-service-lumi.web.cern.ch/cms-service-lumi/brilwsdoc.html (visited on 10/21/2015).

[25] *aix3a sample database*. URL: https://cms-project-aachen3a-datasets.web.cern.ch/cms-project-aachen3a-datasets/aix3adb2/ (visited on 12/13/2015).

[26] BELYAEV, A., CHRISTENSEN, N. D., AND PUKHOV, A. CalcHEP 3.4 for collider physics within and beyond the Standard Model. *Computer Physics Communications* 184, 7 (July 2013), 1729–1769. ISSN: 00104655. DOI: 10.1016/j.cpc.2013.01.014. URL: http://linkinghub.elsevier.com/retrieve/pii/S0010465513000313 (visited on 10/27/2015).

[27] SJÖSTRAND, T., MRENNA, S., AND SKANDS, P. PYTHIA 6.4 physics and manual. *Journal of High Energy Physics* 2006, 5 (May 9, 2006), 026–026. ISSN: 1029-8479. DOI: 10.1088/1126-6708/2006/05/026. URL: http://stacks.iop.org/1126-6708/2006/i=05/a=026?key=crossref.7fbc8fa1a47a48f7565bead655446685 (visited on 10/27/2015).

[28] THE CMS COLLABORATION *SWGuideMuonIdRun2 < CMS < TWiki*. URL: https://twiki.cern.ch/twiki/bin/viewauth/CMS/SWGuideMuonIdRun2#Tight_Muon (visited on 10/24/2015).

[29] THE CMS COLLABORATION Performance of CMS muon reconstruction in pp collision events at $\sqrt{s}$ = 7 TeV. *Journal of Instrumentation* 7, 10 (Oct. 5, 2012), P10002–P10002. ISSN: 1748-0221. DOI: 10.1088/1748-0221/7/10/P10002. URL: http://stacks.iop.org/1748-0221/7/i=10/a=P10002?key=

crossref.73b2ce6e506b977fac02d684318ec472 (visited on 12/12/2015).

[30] THE CMS COLLABORATION *SWGuideMuonId < CMSPublic < TWiki*. URL: https://twiki.cern.ch/twiki/bin/view/CMSPublic/SWGuideMuonId?rev=60#Muon_Isolation (visited on 10/24/2015).

[31] THE CMS COLLABORATION *JetID < CMS < TWiki*. URL: https://twiki.cern.ch/twiki/bin/viewauth/CMS/JetID#Recommendations_for_13_TeV_data (visited on 10/24/2015).

[32] SALFELD, J., REDONDO, I., AND PALMER, C. LUMI POG Report, 25ns Luminosity Update. URL: https://indico.cern.ch/event/463929/session/4/contribution/90/attachments/1202469/1750991/LUMPOG_20151209_update.pdf.

[33] THE CMS COLLABORATION *SWGuideHiggsAnalysisCombinedLimit < CMS < TWiki*. URL: https://twiki.cern.ch/twiki/bin/viewauth/CMS/SWGuideHiggsAnalysisCombinedLimit#Computing_limits_with_the_asympt (visited on 11/02/2015).

[34] READ, A L Modified frequentist analysis of search results (the *CL_{s}* method) (2000). DOI: 10.5170/CERN-2000-005.81. URL: http://dx.doi.org/10.5170/CERN-2000-005.81 (visited on 11/02/2015).

[35] BERINGER, J., ET AL. Review of Particle Physics. *Physical Review D* 86, 1 (July 20, 2012). ISSN: 1550-7998, 1550-2368. DOI: 10.1103/PhysRevD.86.010001. URL: http://link.aps.org/doi/10.1103/PhysRevD.86.010001 (visited on 01/07/2016).

[36] *Search for RPV SUSY resonant second generation slepton production in same-sign dimuon events at $\sqrt{s}$ = 8 TeV*. Tech. rep. AN2013_225_v11. 2013. URL: http://cms.cern.ch/iCMS/jsp/openfile.jsp?tp=draft&files=AN2013_225_v11.pdf.

[37] *LumiPublicResults < CMSPublic < TWiki*. URL: https://twiki.cern.ch/twiki/bin/view/CMSPublic/LumiPublicResults#2015_Proton_Proton_13_TeV_Collis (visited on 11/29/2015).